Study on Buckling of Stiff Thin Films on Soft Substrates as Functional Materials

by

Teng Ma

A Dissertation Presented in Partial Fulfillment
of the Requirements for the Degree
Doctor of Philosophy

Approved March 2014 by the
Graduate Supervisory Committee:

Hanqing Jiang, Chair
Hongyu Yu
Hongbin Yu
Poh Chieh Benny Poon
Jagannathan Rajagopalan

ARIZONA STATE UNIVERSITY

May 2014

ABSTRACT

In engineering, buckling is mechanical instability of walls or columns under compression and usually is a problem that engineers try to prevent. In everyday life buckles (wrinkles) on different substrates are ubiquitous -- from human skin to a rotten apple they are a commonly observed phenomenon. It seems that buckles with macroscopic wavelengths are not technologically useful; over the past decade or so, however, thanks to the widespread availability of soft polymers and silicone materials micro-buckles with wavelengths in submicron to micron scale have received increasing attention because it is useful for generating well-ordered periodic microstructures spontaneously without conventional lithographic techniques.

This thesis investigates the buckling behavior of thin stiff films on soft polymeric substrates and explores a variety of applications, ranging from optical gratings, optical masks, energy harvest to energy storage.

A laser scanning technique is proposed to detect micro-strain induced by thermomechanical loads and a periodic buckling microstructure is employed as a diffraction grating with broad wavelength tunability, which is spontaneously generated from a metallic thin film on polymer substrates.

A mechanical strategy is also presented for quantitatively buckling nanoribbons of piezoelectric material on polymer substrates involving the combined use of lithographically patterning surface adhesion sites and transfer printing technique. The precisely engineered buckling configurations provide a route to energy harvesters with extremely high levels of stretchability.

This stiff-thin-film/polymer hybrid structure is further employed into electrochemical field to circumvent the electrochemically-driven stress issue in silicon-anode-based lithium ion batteries. It shows that the initial flat silicon-nanoribbon-anode on a polymer substrate tends to buckle to mitigate the lithiation-induced stress so as to avoid the pulverization of silicon anode.

Spontaneously generated submicron buckles of film/polymer are also used as an optical mask to produce submicron periodic patterns with large filling ratio in contrast to generating only ~100 nm edge submicron patterns in conventional near-field soft contact photolithography.

This thesis aims to deepen understanding of buckling behavior of thin films on compliant substrates and, in turn, to harness the fundamental properties of such instability for diverse applications.

To my Mom

and

Grandma.

ACKNOWLEDGMENTS

I would like to express my deepest gratitude to my supervisor, Prof. Hanqing Jiang, for his mentorship, guidance and support during the four and a half years. His contagious enthusiasm and perseverance for research have been the constant driving force for my progress. He was always available in the office for discussion and promptly answered your emails despite his busy schedule. I feel very fortunate to have been his student, and therefore to have had such an enjoyable and fulfilling graduate school experience.

I would also like to deeply thank my co-supervisor, Prof. Hongyu Yu, who was abundantly helpful and offered invaluable assistance and guidance to my experimental projects. Without his encouragement and support, I would never step into the experimental fields where I have explored completely different potentials of myself.

I would also like to thank Prof. Hongbin Yu and Dr. Benny Poon for their guidance and support for Intel SRS project during the two and a half years. I have also vastly benefitted from discussions with them in our monthly meetings.

I would like to thank Prof. Jagannathan Rajagopalan for making time to serve on my committee and for enhancing my knowledge by his questions and comments.

I would also like to thank my colleagues in Prof. Jiang's group: Dr. Cunjiang Yu, Dr. Yonghao An, Dr. Jiaping Zhang, Dr. Huiyang Fei, Dr. Qiang Liu, Dr. Zheng Duan, Yuping Pan, Dr. Yong Wang, Dr. Rongjun Zhang, Prithwish Chatterjee, Joseph Shaffer, Amit Abraham, Swathisri Kondagari, Zeming Song, Cheng Lv, Xu Wang, Yiling Fan, Tianwei Sun, Deepakshyam Krishnaraju.

I would also like to thank my other collaborators: Hanshuang Liang, Rui Tang, Hai Huang, Dr. Xiaotun Qiu, Dr. Oiler Jonathon, Bryce Carande, Mengbing Liang, George Chen, Ruirui Han.

I would also like to convey thanks to China Scholarship Council for providing financial support.

Most importantly, I would like to thank my parents and my sister. Their encouragement and never-ending support throughout my entire life made everything easier to achieve.

TABLE OF CONTENTS

Page

Page

Page

LIST OF TABLES

Table Page

LIST OF FIGURES

Figure Page

Figure Page

Figure Page

Figure Page

Figure Page

Figure Page

Figure Page

CHAPTER 1

Introduction

The first chapter of this thesis will introduce the background and motivation for the current study.

1.1 Introduction

Mechanical instability is usually a problem that engineers try to prevent. Such instabilities can often lead to structural failures and collapses. For example, buckling is a type of elastic instability which can disappear/reappear by the application of an external force. In engineering, buckling is instability of walls or columns under compression. And when a wall buckles, the collapse is usually sudden and catastrophic.

Over the past decade or so, however, researchers have begun to embrace instability, in a more flexible way, thanks to the widespread availability of soft polymers and silicone materials. The large deformation of soft materials is harnessed to explore various elastic instabilities [1], including buckling [2, 3], creasing [4-6], and crumpling[7]. And soft materials do not provide functions alone but integrate with hard materials working in a hybrid form. Especially buckling instability has been extensively discussed and manipulated in a way that offers deterministic control over the geometries including pattern order, wavelength and amplitude.

For example, one can generate buckling instability by buckling a bilayer structure, where a thin hard film coated on top of an expanded thick compliant film undergoes a compressive force. The compressive strain in the hard film can be provided either by a mechanical strain or by cooling its present state down to its equilibrium stress-free state [2, 8].

1.2 Mechanism of surface buckling

Buckling (or wrinkling) is a commonly observed mechanical instability phenomenon typically treated as a nuisance. In recent years, researchers have proposed

the use of ordered buckling structures of stiff thin films on soft substrates with wavelengths in the nanometer to micrometer order, in a broad spectrum of applications, such as, microfluidic devices [9], templates for cell guidance [10, 11] and colloidal particles assembly [12, 13], stretchable electronic interconnects [14-19], stretchable electronic devices [20-26], modern metrology methods [27], tunable diffraction and phase gratings [9, 10, 28, 29], and methods for micro/nano-fabrication [2, 8, 30, 31].

A stiff thin film is prepared on a thick, less stiff substrate (Figure 1.1). When the substrate is compressed, the thin film buckles into a sinusoidal shape to relieve the applied stress. In general, to achieve lower energy cost a stiff film tends to buckle in a longer wavelength but a soft substrate favors a shorter wavelength when buckled. When combined into a bilayer, the system will yield a buckling wavelength somewhere between these large and small wavelengths [32].

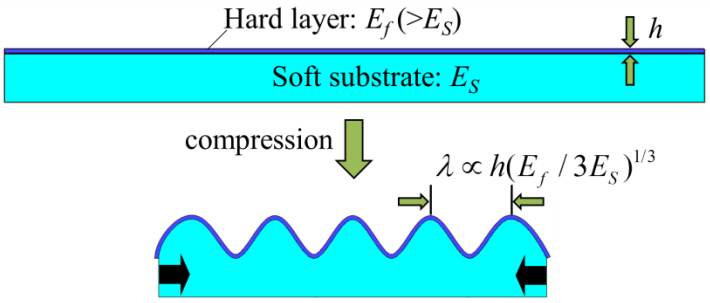

Figure 1.1. Schematics for the buckling of a thin hard film on a compliant substrate. The hard film is supported by a soft elastic substrate. Buckles form on this structure under lateral compressive strain/stress fields.

Energy method is often used for non-linear buckling analysis [33, 34]. The buckling wavelength and amplitude are determined by the intrinsic properties of the films, film thickness and external trigger as a result of the minimization of the total energy of the system (membrane and bending energies of film material, and deformation energy of

substrate). If the prestrain is smaller than ~5%, using small-strain model the wavelength of purely sinusoidal buckling pattern can be expressed as [33, 34]

$$\lambda = 2\pi h\left(\frac{\bar{E}_f}{3\bar{E}_s}\right)^{1/3} \tag{1.1}$$

Where $\bar{E} = E/(1-\nu^2)$ is the plane-strain modulus, E is Young's modulus and ν is Poisson's ratio. The subscripts "*f*" and "*s*" refer to the hard thin film and the soft substrate, respectively. Equation (1.1) suggests that buckling wavelength depends only on the film thickness and film/substrate modulus ratio, but not on the prestrain (ε_{pre}) if the prestrain is small enough, up to ~5%. The amplitude of buckling is given by

$$A = h\left(\frac{\varepsilon_{pre}}{\varepsilon_c} - 1\right)^{1/2} \tag{1.2}$$

Where

$$\varepsilon_c = 0.25\left(\frac{3\bar{E}_s}{\bar{E}_h}\right)^{2/3} \tag{1.3}$$

is defined as the critical buckling strain, or the minimum strain needed to induce buckling. Note that both the wavelength and amplitude are linearly proportional to the film thickness and only the amplitude increases with prestrain quadratically. That means, the prestrain is absorbed by the increase of the buckling amplitude, while the wavelength remains constant, which is due to the ignorance of the large deformation of substrate in small-strain model.

For the large-strain (>5%) case, the soft substrate becomes non-linear and the large deformations and geometrical nonlinearity are taken into account, the buckling wavelength and amplitudes can be written [24, 35]

$$\lambda = \frac{\lambda_0}{\left(1+\varepsilon_{pre}\right)\left(1+\xi\right)^{1/3}}, \quad A = \frac{A_0}{\left(1+\varepsilon_{pre}\right)\left(1+\xi\right)^{1/3}}, \quad \xi = 0.15625\varepsilon_{pre}\left(1+\varepsilon_{pre}\right) \quad (1.4)$$

Here, λ_0 and A_0 are the wavelength and amplitude, respectively, for the small-strain case, as given by Eq. (1.1) and (1.2). And $(1+\xi)^{1/3}$ arises from the geometrical non-linearity (large deformation) and non-linear constitutive model for the substrate.

In this bilayer system two criteria must be met so as to buckle the top layer. The in-plane compressive stress in the thin film cannot be too small to buckle the film and the substrate must be compliant enough to allow out-of-plane deformation to accommodate the deformation of the top layer. A wide variety of hard films on soft elastomeric substrates have been studied as shown in Figure 1.2.

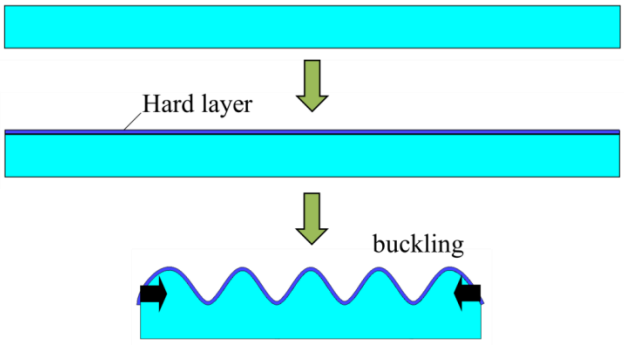

Soft substrate	Hard layer formation	Compressive strain field
PDMS [2, 8] GEL [36, 37] PS [38, 39] PMMA [40]	Surface oxidation • UV/Ozone [19] • oxygen plasma [8] Thin film deposition[2, 41] Thin film transfer[42-44]	Mechanical stress [42, 43] Thermal stress • cooling [2, 8] • heating [45, 46] Osmotic stress [47, 48] Electrochemical stress [49]

Figure 1.2. Several methods for preparing micro-buckles.

The typical soft substrates include poly(dimethylsiloxane) (PDMS), hydrogel and glassy polymer such as polystyrene (PS) and poly(methyl methacrylate) (PMMA) (Figure 1.2). In the experiments presented in this thesis, PDMS elastomer is used as the soft substrate in that it is optically transparent, flexible, low-cost and doesn't break. Also PDMS is unique in that, when freshly plasma-oxidized, it can be bonded to itself and other materials, such as silicon, without an adhesive, and almost every other polymer requires an adhesive [50].

There are three main methods for hard film fabrication. (1) An oxide skin layer that act as the thin film can be generated directly on PDMS surface either by oxygen plasma treatment or UV/ozone (UVO) exposure. These treatments are known to convert the PDMS surface into a thin layer of glassy silicate (SiO_x), which can be directly bond chemically with the thin Si film. (2) Direct deposition of a hard thin layer, such as Au and Si, onto a soft expanded substrate. (3) A thin film is separately prepared on donor substrate and then heterogeneously "borrowed" onto a compliant PDMS substrate via transfer printing. By applying the same treatments from (1) PDMS can directly bond with thin film, which might be the most unique aspect of PDMS polymer that makes academic community embraces it. All these methods enable the thickness of thin film in the range of submicron and therefore control the wavelength of the micro-buckles easily ranging from hundred nanometers to tens of micrometers [51]. The buckles are triggered by the exertion of lateral compressive strain or stress including mechanical, thermal, osmotic and electrochemical stresses (Figure 1.2) [52].

1.3 The goal and outline of this thesis

The goal of this thesis is to deepen understanding of buckling behavior of thin films on PDMS elastic substrates and, in turn, to harness the fundamental properties of such instability for diverse applications. This thesis consists of four main chapters. Chapter 2 describes a strain sensing technique that utilizes wrinkling patterns on PDMS as an optical grating to measure the thermally-induced strain of different materials. Chapter 3 describes a method to utilize pre-patterned ZnO nanoribbons on soft substrates to achieve buckled forms for stretchable energy harvesting applications within audio frequency range. Chapter 4 describes the use of silicon thin films on soft substrates as anodes to circumvent the electrochemical-reaction-induced stress problem by buckling in lithium ion batteries. Chapter 5 describes a near-field photolithographic approach that uses wrinkled PDMS as submicron masks to generate simple submicron structures.

Chapter 2

Micro-strain sensing using wrinkled stiff thin films on soft substrates as tunable optical gratings[†]

We propose a strain sensing approach that utilizes wrinkled patterns on PDMS as an optical grating to measure thermally-induced strain of different materials. The mechanism for the strain sensing and the effect of PDMS grating on strain sensing are discussed. By bonding the PDMS grating onto a specimen, the coefficient of thermal expansion (CTE) of the specimen can be deduced by measuring the diffraction angle change due to the change in PDMS grating periodicity when thermal strain is introduced. The measured CTEs agree well with the known reference values.

[†] Based on Teng Ma[*], Hanshuang Liang[*], George Chen, Benny Poon, Hanqing Jiang, and Hongbin Yu. "Micro-strain sensing using wrinkled stiff thin films on soft substrates as tunable optical grating." Optics Express 21.10 (2013): 11994-12001. ([*]: Equal contribution) and Hanshuang Liang[*], Teng Ma[*], Hoa Nguyen, George Chen, Hao Wu, Hanqing Jiang, and Hongbin Yu. "High Sensitivity In-Plane Strain Measurement Using a Laser Scanning Technique." Electronic Components and Technology Conference (ECTC), 2014 IEEE 64rd. IEEE, 2014. ([*]: Equal contribution)

2.1 Introduction

Nowadays electronic packaging involves multiple scales ranging over several orders of magnitude. For example, the silicon chips in flip-chip applications typically have dimensions of several mm on a side and the corresponding printed circuit board has dimensions of many cm on a side and the solder joints have typical heights of 50-100μm [53]. As a result, when subjected to temperature changes, the large CTE mismatch leads to uneven expansions between different components that can cause severe deformation and strains, for example, in the solder joints. So there is a great need for characterizing components deformations and strains at micron range due to thermo-mechanical loadings caused by CTE mismatches.

The full-field optical methods of micro Moiré and digital image correlation (DIC) are well suited for measuring two-dimensional (in-plane) thermomechanical deformations of electronic packaging, and have been widely applied to charactering strains in solder joints [53]. Micro Moiré [54-58] is a highly sensitive, full-field in-plane sensing technique but the illuminated area for generating a Moiré pattern needs to be large enough to detect small strain, consequently lacking the ability to resolve strain within small spatial variation. DIC techniques [59-63] can achieve high spatial resolution with high in-plane displacement resolution but the field of view is compromised since a large optical magnification is required and becomes a limiting factor when detailed strain mapping in a large area is needed. We propose an in-plane micro-strain characterization technique by scanning a laser on diffraction gratings so as to fill the technology gap between traditional DIC and Moiré technique with a high strain sensitivity, high spatial resolution and large field-of-view.

Currently, diffraction gratings are conventionally manufactured using two methods. The first method is the use of ruling engines in a diamond turning technique, where a high precision stage equipped with diamond tips is used in the manufacturing process. This method however, is a serial process, and is typically slow and expensive. The second method utilizes laser technology. Diffraction gratings made this way are called holographic gratings and have sinusoidal grooves. They are rigid and not tunable.

We also propose a novel grating manufacturing technique by using a buckled thin stiff film on soft substrates as a grating, which has distinct advantages over the two methods mentioned above. The proposed technique employs the use of a much simpler manufacturing process which only involves a mechanical straining process on soft substrates (e.g., PDMS) and a routine nano thin metal (e.g., Au) deposition step. PDMS is elastic and compliant enough so that its presence does not significantly alter the deformation of the specimen. The simplicity of the fabrication steps allows the proposed technique to have significant cost advantage over conventional methods.

Here PDMS/Au gratings are utilized as tunable strain sensors. A PDMS/Au grating is first attached to the specimen of interest. Any change to the strain of the specimen (thermally or mechanically induced) is imparted to the grating and changes its periodicity. The strain sensing mechanism relies on the detection of the variation in the diffraction angle of the laser beam shinning on the surface of the tunable grating. The variation in diffraction angle can then be related to the strain induced by the specimen of interest. The proposed tunable strain sensor and its detection mechanism are expected to have high strain sensitivity in capturing the strain variations within specimen.

2.2 Fabrication of PDMS/Au grating

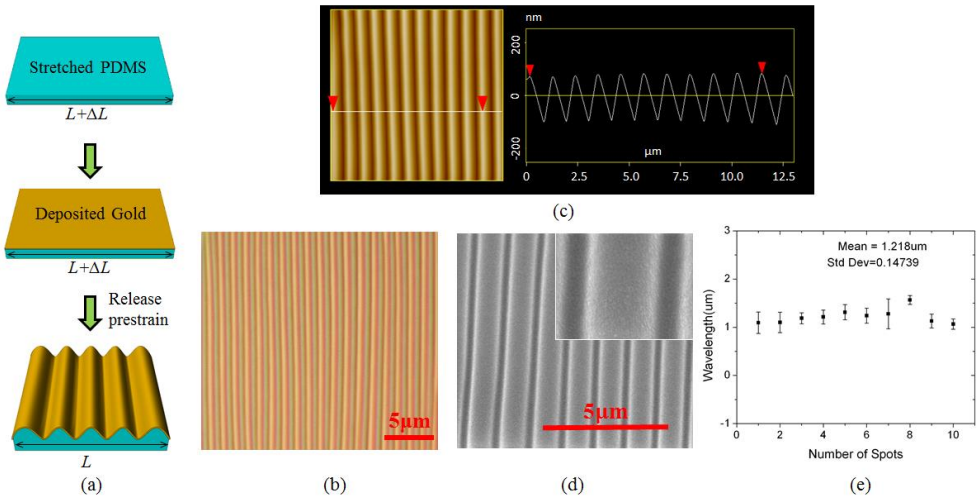

Figure 2.1. (a) Schematic of the fabrication process for PDMS/Au grating. (b) Optical microscopy image and (c) AFM image of wrinkling profile of PDMS/Au grating surface. (d) SEM image of wrinkles. (e) Wrinkling wavelength (period) distribution at ten different spots over a surface area of 100 × 100 μm^2. The wrinkling period remains largely constant over this surface area, in good agreement with the calculated period value by Eq. (1). The error bars are one standard deviation of the data, which is taken as the experimental uncertainty of the measurement.

Figure 1(a) illustrates the fabrication flow of the PDMS/Au grating. A PDMS elastomer (Sylgard 184, Dow Corning) was made by mixing the base component and the curing agent in a 10:1 ratio by weight, followed by de-gassing and curing at 80˚C for 3 hours. A slab of PDMS elastomer (0.1-1 mm thick) was mounted and elastically stretched by a home-made stage with designed uniaxial pre-strain. After being exposed to oxygen plasma (50 W) for 1 minute to enhance the adhesion, the pre-strained PDMS slab was sputter-coated with a gold (90%)/palladium (10%) (Au/Pd) alloy film of nanoscale thickness. The addition of palladium to gold increases its bonding strength, known as white gold. Due to the small proportion of palladium we will refer to the alloy as gold. Finally, the relaxation of the pre-strain in the PDMS substrates compresses the Au thin

film, leading to the deformation and wrinkling in both the Au film and PDMS substrate surface in a sinusoidal pattern. This is a result of the minimization of the system's potential energy by the out-of-plane deformation. The wrinkling period, *d*, is determined by the mechanical properties of Au film and PDMS substrate, the pre-strain ε_{pre}, and the thickness of the gold film, as described previously [29]

$$d = \frac{2\pi h_f}{\left(1+\varepsilon_{pre}\right)\left(1+\xi\right)^{1/3}}\left[\frac{E_f\left(1-\upsilon_s^2\right)}{3E_s\left(1-\upsilon_f^2\right)}\right]^{1/3} \tag{2.1}$$

where h_f is the thickness of the Au film, E is Young's modulus and v is Poisson's ratio. The subscripts "s" and "*f*" refer to the PDMS substrate and Au film, respectively. By varying the pre-strain ε_{pre} and the Au film thickness h_f, the buckling period *d* can be tuned with a broad range. In this work, the buckling period is in the order of micron or submicron range for the optimal grating efficiency for the visible light, which is employed for strain sensing application as discussed below.

Figure 2.1(b) shows an optical microscope image of a PDMS/Au grating fabricated by the above mentioned method, with h_f = 10 nm, ε_{pre} = 15%, and the measured buckling period *d* = 1.22 μm, which agrees well with the calculated value of 1.20 μm obtained from Eq. (2.1) when the following material parameters are used, E_f = 80 GPa, Es = 2 MPa, h_f = 10 nm, v_f = 0.3, and v_s = 0.4921. Fig. 1(c) shows the atomic force microscope (AFM) image of the grating topography and a line-scan profile, which illustrates the uniformity of the buckling in a small area. Figure 2.1(d) illustrates scanning electron microscope (SEM) image of the continuous gold film along wave direction on PDMS. To examine the uniformity over a large area, the buckling periods were measured

at ten different locations on an area of 100×100 μm^2 and the results are shown in Figure 2.1(e). It was found that the buckling period is uniform over a large area.

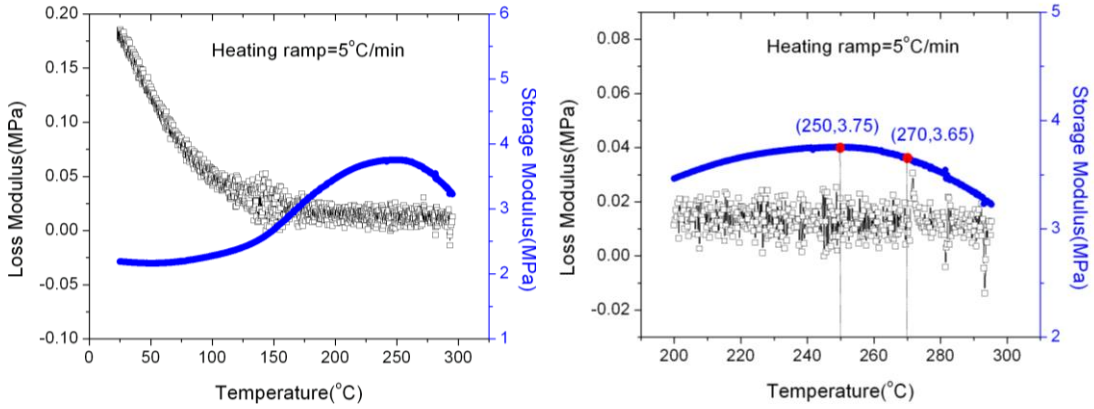

(a) (b)

Figure 2.2 A temperature sweep test on PDMS. Storage Modulus and Loss Modulus against temperature are plotted. (a) from room temperature to 290˚C. (b) from 200˚C to 290˚C.

Dynamic mechanical analysis (DMA) is applied for mechanical property testing at high temperature. Over a large temperature range from room temperature to 290 ˚C the storage modulus of PDMS is always larger than the loss modulus which indicates that PDMS is still solid at high temperature (Figure 2.2(a)). From 250 ˚C to 270 ˚C, the storage modulus only dropped a little bit (Figure 2.2(a)). We also heat the PDMS winkles up at 260˚C for half hour and found that the wrinkles did not disappear. Therefore PDMS grating is stable for high temperature.

2.3 Operation principle

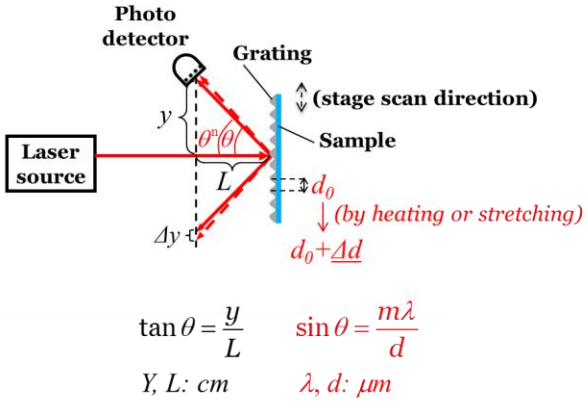

Figure 2.3. Schematic of the setup for strain sensing using buckled thin film grating

A highly sensitive optical diffraction approach was developed to measure strain on the specimen of interest. By using a PDMS/Au grating attached to different specimens (for example, a silicon substrate), a minuscule change in strain within the specimen can be detected with a large change in displacement measured by the photo detector. This mechanism starts from the simple diffraction equation, $d_0\sin\theta = m\lambda$, which relates the diffraction angle θ, initial grating period d_0, and laser source wavelength λ, m is the order of diffraction, when laser beam is normal to the grating surface. As shown in Figure 2.3, the optical setup for strain measurement, a geometric relation, $\tan\theta = y/L$, relates the horizontal position L of the specimen and vertical position y of the photo detector.

When a strain is induced on the specimen through either mechanical or thermal means, the grating period changes from d_0 to d (= d_0 + Δd) and leads to the change in diffraction angle θ by $\Delta\theta$. Meanwhile, the change of θ results in the change of y by Δy, which linearly depends on Δd, as shown below,

$$\Delta y = -\frac{\lambda L}{d_0^2\left(1-\frac{m^2\lambda^2}{d_0^2}\right)^{3/2}}\Delta d = -\frac{\lambda L}{d_0\left(1-\frac{m^2\lambda^2}{d_0^2}\right)^{3/2}}\varepsilon = -A\varepsilon. \qquad (2.2)$$

Where the strain ($\varepsilon = \Delta d / d_0$) of the specimen is related to Δy by the pre-factor A.

When L is in the order of 10 cm, and the buckling period d_0 and light wavelength λ, both in the order of submicron ($m\lambda < d_0$), the magnification factor A is approximately 1×10^7 μm. To put this in perspective, one micro-strain (10^{-6}) leads to a 10 μm change in the vertical position y of the photo detector, which is significantly much easier to be measured. In addition, this magnification factor, A, can be further amplified by properly choosing a d_0 that approaches λ (Eq. (2.2)). This simple mechanism of magnification forms the basis of this highly sensitive strain measurement technique.

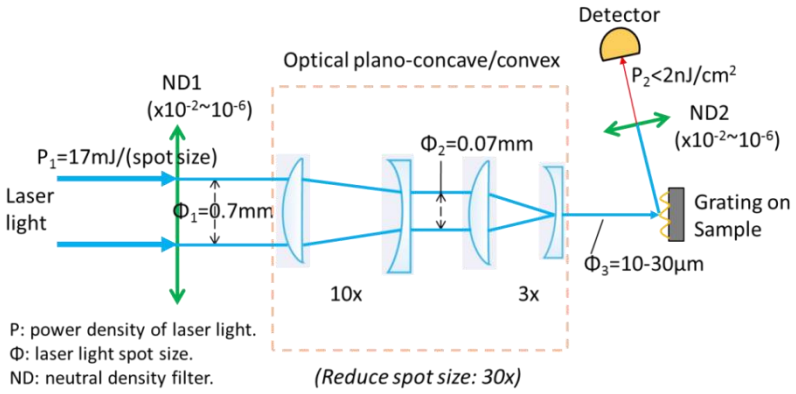

Figure 2.4. Schematic of optical setup for micro-strain sensing

Figure 2.4 illustrates the optical setup used in the micro-strain sensing. The light source was a 633 nm He-Ne laser with output power of 21 mW. The laser spot size had been reduced from 700 μm (Φ_1) to 200 μm (Φ_2) in diameter at the grating surface through the use of two optical lenses. In order to improve the signal to noise ratio, an optical chopper was placed before the series of optical lenses to synchronize with the

optical detector. A 50/50 beam splitter generated a reference light signal which was fed into an auto balanced photo detector. The photo detector compared the first order diffracted beam from the grating with the reference light to improve the signal-to-noise ratio for high sensitivity.

Two types of specimen have been tested to demonstrate the capability of this strain sensing technique. One is a single homogenous material for testing strain sensitivity and the other is a composite of two dissimilar materials for obtaining spatial resolution of this technique.

2.4 Micro-strain testing for a single homogenous material

The strain sensitivity is tested using a single homogenous material as a specimen (Figure 2.5). When subjected to a temperature change, the grating expands and the grating period changes accordingly so the CTE of the specimen material can be deduced from its thermal strain.

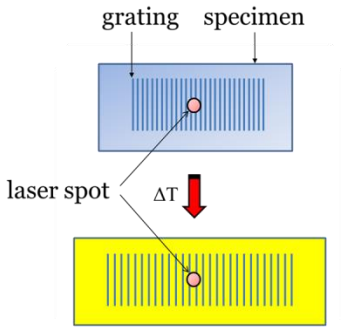

Figure 2.5. Schematic of micro-strain sensing for a single homogenous material

2.4.1 The effect of grating dimension

CTE of PDMS is around 300 ppm/˚C which is much higher than most of electronic packaging materials such as silicon (2.6 ppm/˚C) and copper (17 ppm/˚C). By attaching PDMS gratings on, for example, silicon, we want to deduce the strain of silicon from the strain of PDMS grating. Can ε_{PDMS} reflect $\varepsilon_{silicon}$ accurately? Or, in other words, what's the effect of PDMS dimension on strain measurement?

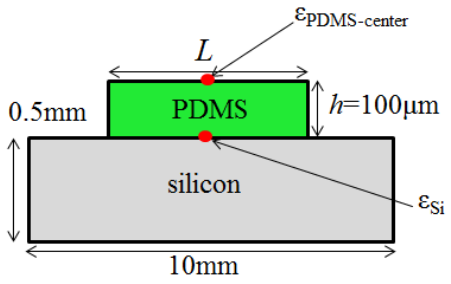

Figure 2.6. Schematic of a PDMS grating attached on a silicon specimen

The commerical finite element package ABAQUS [64] was used to study the effect of the dimension of a PDMS grating on the strain measurment. Figure 2.6 shows the model, including a PDMS grating with a thickness of 100 μm and length L on top of a 0.5 mm thick, 10 mm long silicon specimen. Thermal stress analysis is conducted by introducing a uniform temperature change ΔT. The PDMS and the silicon specimen are modeled by 4-node plane strain temperature-displacement coupled elements (CPE4T). The PDMS-Si interface is treated as shared nodes. The bottom of the silicon substrate is confined. The top Au layer is not considered in the finite element analysis because its thickness is negligible (10 nm). The following material parameters are used in the analysis [65]: E_{PDMS} = 2 MPa, ν_{PDMS} = 0.5, $\alpha_{PDMS} = 310\times10^{-6}$ /˚C, E_{Si} = 130 GPa, ν_{Si} = 0.3 , $\alpha_{Si} = 2.6\times10^{-6}$ /˚C, ΔT = 50˚C, where α is the coefficient of thermal expansion (CTE).

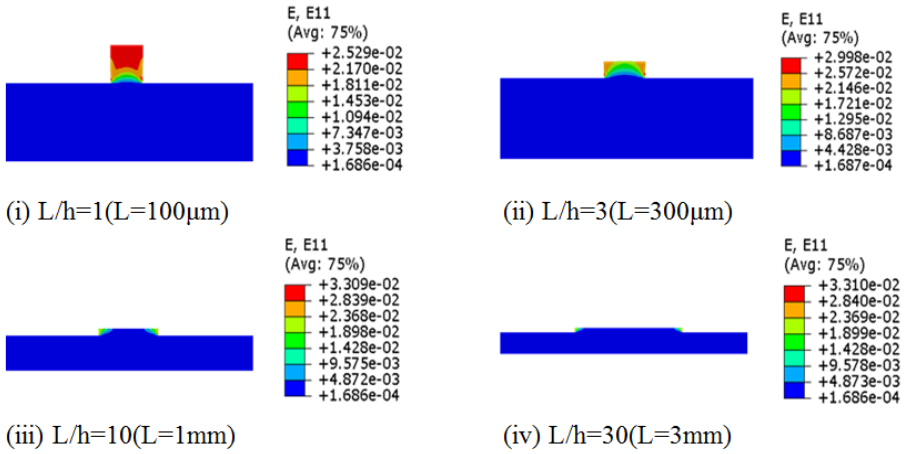

Figure 2.7. Strain coutour in the horizontal direction for different ratios of PDMS lengths (L) and a constant thickness (h=100 μm)

Strain contours in the horizontal direction for different ratios of PDMS length and thickness are shown in Figure 2.7. For L/h = 1, the strain at the top surface of the center of the PDMS (ε_{PDMS}) is about two order of magnitude higher than the strain at the top of the silicon specimen (ε_{Si}). The explanation for this is that for a small L/h ratio, the constraint from the underlying silicon specimen is too weak. Therefore, the strain at the top of the PDMS grating, in this case, only reflects the PDMS itself and not the underlying silicon. As the L/h ratio increases, the constraint from the silicon substrate is increased and the strain at the top of the PDMS grating begins to resemble more and more like the strain of underlying silicon specimen of interest, as can be seen in Figure 2.7. For an L/h ratio of 30, the strain of the PDMS grating is equal to the strain of the underlying silicon specimen of interest over 80% of the entire surface area of the PDMS grating. In this scenario, the detected strain ε_{PDMS} reflects the actual strain ε_{Si}.

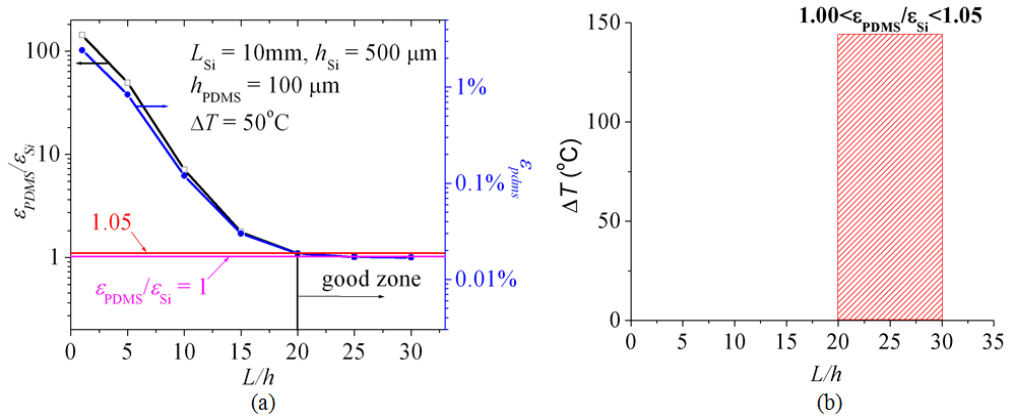

Figure 2.8. (a) $\varepsilon_{pdms}/\varepsilon_{silicon}$ and ε_{pdms} as a function of *L/h*. (b) Phase diagram of $\varepsilon_{pdms}/\varepsilon_{silicon}$

Figure 2.8(a) shows the ratio of ε_{PDMS} and ε_{Si} as a function of *L*/*h* ratio for PDMS grating on Si specimen. It can be seen that when the *L*/*h* ratio exceeds a critical value of 20, the ε_{PDMS} reflects ε_{Si} with only a 5% error. Figure 2.8(b) shows that this relation (i.e., *L*/*h* > 20) holds for all temperature change due to the linearity of this relation. In fact, this analysis is likely to provide an upper bound of the *L*/*h* ratio because the CTE mismatch between silicon and PDMS is likely to be more severe than most conventional metals and polymers. However, note that for materials with a smaller CTE than silicon, such as, glass and other low CTE ceramics, the critical value for *L*/*h* ratio can be smaller than 20.

2.4.2 Measurement results

Thermal strains of three different homogenous materials (PDMS, copper and silicon) with differing CTE spanning three orders of magnitude are measured to verify the micro-strain sensing technique with tunable PDMS/Au gratings. PDMS/Au gratings are bonded on specimens that are heated up by a copper block, as shown in Figure 2.9(a). A thermal couple is attached to the copper block to form a feedback system for the temperature control. In this system, the temperature reading on the specimen is calibrated

to be within one degree of accuracy, and the temperature range for the strain measurement is between room temperature and 65 ˚C. The laser spot size is 200 μm.

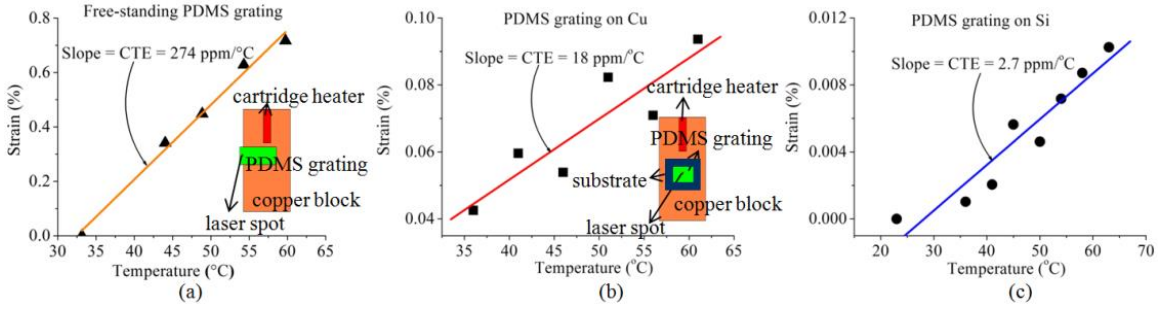

Figure 2.9. Measured CTEs for (a) freestanding PDMS, (b) copper and (c) silicon. Insets are the schematics of the setup for thermal micro-strain measurement.

The first specimen is a freestanding PDMS grating, which is hanging over at the edge of the copper block, as shown in the inset schematic in Figure 2.9(a). The focused laser spot is located just off the copper block to measure the thermal strain of the PDMS grating without constraints from the copper block. Figure 2.9(a) shows the measured strain as a function of temperature for this freestanding PDMS grating, where a good linearity is observed. The CTE of PDMS, i.e., the slope of strain/temperature relation, is 274 ppm/˚C (part per million per degree Celsius), which agrees with the reference value of the CTE of PDMS, 265 ppm/˚C, measured using commercial thermal-mechanical analysis tool Q400 from TA instruments, under expansion mode at 10 mN force.

The second specimen is a piece of copper sheet, on which the PDMS/Au grating is attached by a thin double-sided adhesive tape. The size of PDMS/Au grating has been chosen based on Figure 2.9(a) to ensure the measured strain on top of the grating accurately reflects the strain of copper substrate. Figure 2.9(b) shows the strain-temperature relation. The CTE of copper given by the slope is obtained as 18.2 ppm/˚C, which is consistent with the CTE of copper (17.5 ppm/˚C) [66]. Some of the data points

in Figure 2.9(b) are scattered compared to Figure 2.8(a), which can be attributed to the bonding quality of the adhesive tape between copper and PDMS.

The last specimen is a silicon substrate. The PDMS/Au grating can be firmly bonded to the Si substrate by treating the Si surface with oxygen plasma to form a SiO_2 bond between the PDMS and Si [67]. Si has a much lower CTE (2.6 ppm/˚C), compared to previous two specimen materials. The experimental data is plotted in Figure 2.9(c), which gives an extracted CTE value of 2.73 ppm/˚C, very close to the reference value of the CTE of silicon. The measured data here show much less fluctuation than the data from the PDMS bonded to copper as the result of much better bonding quality between Si and PDMS. The temperature step here is 5C thus the smallest deformation we can measure is around 10 μm, thus demonstrating the sensitivity at the level of 10^{-5}.

2.5 Micro-strain testing for two-dissimilar-material composite

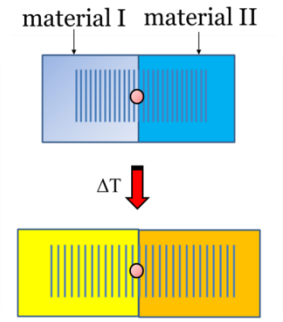

Figure 2.10. Schematic of micro-strain sensing for two dissimilar materials composite

Spatial resolution of this sensing technique is obtained through testing a composite of two dissimilar materials. Upon thermal loading, a strain change occurs when laser is scanning cross the junction due to the CTE mismatch between two materials.

2.5.1 The effect of grating thickness

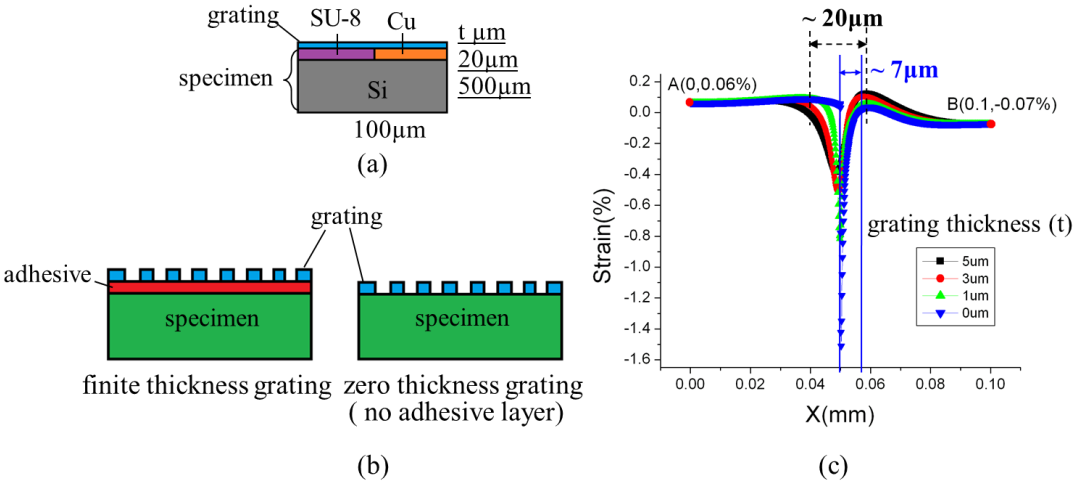

Figure 2.11. (a) Schematic of a grating attached on a SU-8/Cu composite specimen. (b) Schematic of a finite thickness grating and a 'zero-thickness' grating. (c) Strain as a function of the horizontal distance on the top of the grating. Here the temperature change ΔT is 50 ˚C.

Although we want to measure the strain of the surface of the specimen, we actually measure the strain of the surface of the specimen grating. The difference can be very significant when it comes to micro-mechanics analyses for a composite specimen. Finite element analysis is used to simulate the thermal deformation scenario. A grating is attached on top of a SU-8/copper composite, which is mounted on a silicon substrate, as shown in Figure 2.11(a). When subjected to a temperature change, we expect that the junction experiences a sudden strain change due to the CTE mismatch between SU-8 and copper. By varying the thickness of the grating from 0 to 5 μm, the strain distribution on the grating surface is calculated as plotted in Figure 2.11(c). It is observed that when the grating thickness is zero there is a sharp jump of strain over a range of 7 μm long (blue curve). When the grating thickness increases to 5 μm, the strain only jumped a little bit over a much wider range 20-μm-long (black curve). Obviously, finite thickness grating

will smear out the strain information from the specimen as strains are attenuated and redistributed when transmitting through the grating thickness, which is known as shear lag effect [68]. Therefore, there is a need for zero thickness gratings fabricated on specimen to reflect the real strain on specimen as shown in Figure 2.11(b).

2.5.2 Zero-thickness gratings

Zero-thickness gratings are amplitude gratings comprised of reflective metal bars and relatively non-reflective spaces [68, 69]. They are in fact zero thickness since the metal bars are extremely thin (tens of nm) and the spaces are actually zero thickness. This zero thickness grating consisting of ultra-thin reflective metal bars circumvent the shear lag problem of finite thickness gratings and can be used for 1-D strain sensing.

Many different methods exist for fabrication of zero thickness gratings. Most of these techniques can be grouped into two main categories: lithographic techniques and direct machining. Lithographic techniques use light-sensitive polymers in conjunction with controlled etching or deposition methods such as electron beam lithography (EBL), deep ultraviolet (UV) and interference lithography to generate submicron feature sizes for gratings. In direct machining, the surface relief structure is produced through direct removal of the specimen material or addition of other material in a controlled manner without any intermediate processes. For example, focused ion beams (FIB) is capable of scribing a grating directly into the specimen material.

All of these methods for generating zero thickness gratings are directly fabrication processes with no need for an adhesive layer in conventional gratings. These processes offer a strong bonding strength between zero thickness gratings and specimen so that the

thin metal bars can move freely to follow the specimen distortions, which makes them attractive candidates for micromechanics studies involving severe strain gradients or material discontinuities, as in fracture studies [68].

In addition to 1D parallel metal bars, cross-line gratings can be generated as zero-thickness spaces in both x and y directions, separating tiny metal dots in a regular orthogonal array for 2D strain sensing application.

2.5.3 Fabrication of a planarized junction of SU-8/Si

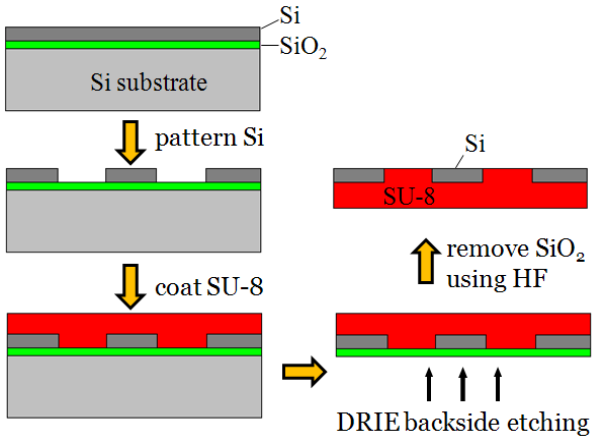

Figure 2.12. Fabrication flow of SU-8/Si junction

In order to obtain the strain information at the junction of two dissimilar materials with different CTEs upon thermal loading, we fabricated a globally planarized junction composed of SU-8/Si as illustrated in Figure 2.12. The fabrication of the SU-8/Si starts from a silicon on insulator (SOI) wafer. The top silicon layer is 10-20 μm thick and is patterned into silicon strips using a standard lithography process. The width of the silicon strips and the spacing are in the range of tens of microns to several hundreds of microns. Then an SU-8 layer is spin-coated on top to fill in the trenches completely. After hard-

baking the SU-8 layer, deep reactive ion etching (DRIE) is used to etch the silicon substrate from the backside until the SiO_2 etch stop layer, which is then removed at the subsequent step using hydrofluoric acid (HF). Figure 2.13 shows the scanning electron microscopy (SEM) image (a) of a SU-8/Si junction and the optical image (b) of a zero thickness grating composed of ultra-thin gold bars on the junction fabricated using EBL and metal lift-off. The optical image doesn't focus well for the up-right-hand corner area since the junction surface is not perfectly flat and exhibits slight amounts of warping induced by the fabrication process.

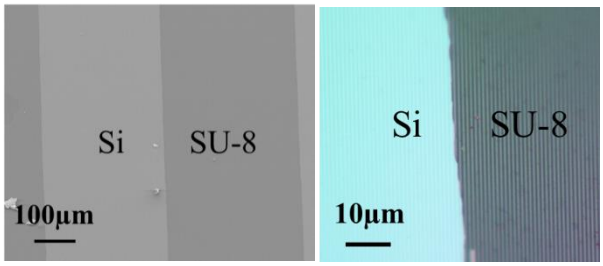

(a) (b)

Figure 2.13. SEM image of (a) SU-8/Si junction and (b) optical image of a zero thickness grating on a SU-8/Si junction using EBL.

We should point out that this silicon surface is coming from the unpolished side of the device layer and is relatively rough compared to the polished silicon surface. As a result the rough surface can abate the reflection of the laser light. Also, the sidewalls of the silicon strips are relatively deep (>10 μm) and therefore are neither vertical nor perfectly smooth due to isotropic dry etching. After filling with the SU-8 and baking it is possible that cracks or delamination at the interface of the sidewalls are present due to the large CTE mismatch between SU-8 and Si.

2.5.4 Finite element analysis of SU-8/Si

The commercial finite element package ABAQUS is used to simulate the thermal deformation of the junction structure of SU-8/Si when subjected to temperature changes. Figure 2.14(a) shows the model, including three 300-μm-wide by 20-μm-thick silicon strips embedded in a 200-μm-thick by 2000-μm-long SU-8 substrate with 300 μm spacing between the strips. The thermal strain analysis is conducted by introducing a uniform temperature change ΔT in the whole domain. The silicon and SU-8 are modeled by a 4-node bilinear plane strain element (CPE4) for two different cases. In case one, the ideal bonding, the SU-8/Si interface is treated as shared nodes which indicates the perfect bonding between the silicon strips and the SU-8 substrate on both the bottom and the two sides. In the latter case, the weak bonding case, the silicon strips are connected to the SU-8 substrate only through the bottom using TIE constraint and there is no bonding with the SU-8 on the two sides of each silicon strip. The weak bonding case is used to simulate a scenario when the bonding is less than ideal and there is delamination on the two sides. The following material parameters are used in the analysis: $E_{SU\text{-}8}$ = 2 GPa, $v_{SU\text{-}8}$ = 0.3, $\alpha_{SU\text{-}8}$ = 52 $\times 10^{-6}$/°C, E_{Si} = 130 GPa, v_{Si} = 0.3, α_{Si} = 2.6 $\times 10^{-6}$/°C, ΔT = 45°C, where E, v and α are Young's modulus, Poisson's ratio and the CTE, respectively. We assume that the surface is ideally flat and there is no warpage existing.

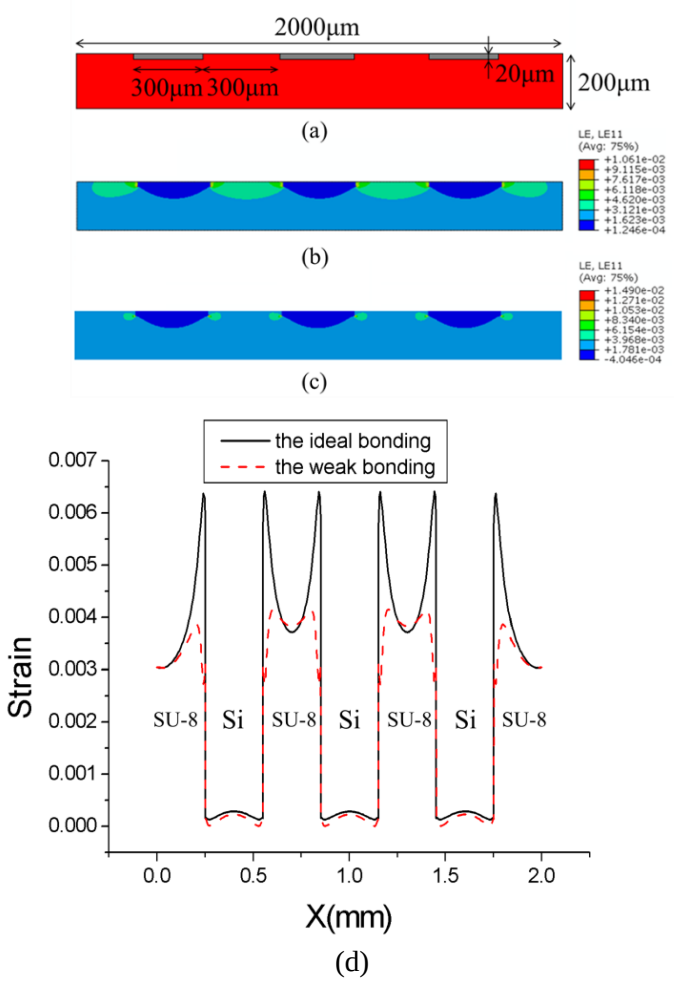

Figure 2.14. (a) Schematic of the SU-8/Si junction structure. (b) Strain contours in the horizontal direction for the ideal bonding case and (c) for the weak bonding case. (d) Strain as a function of the horizontal distance on the top surface of structure. Here the temperature change ΔT is 45˚C.

Strain contours in the horizontal direction are shown in Figure 2.14(b) for the ideal bonding case and (c) for the weak bonding case. Figure 2.14(d) shows the strain as a function of horizontal distance on the top surface of the junction structure for the two cases. The strain on the SU-8 area is much higher than that of the silicon strips and when subject to a temperature change of 45 ˚C, the junction experiences a sudden strain change due to the CTE mismatch. The strain on the silicon surface fluctuates slightly and the two ranges are at the same level for both cases: 1.3×10^{-4}~2.9×10^{-4} for the ideal bonding

case and 8×10^{-6}~2.3×10^{-4} for the weak bonding case. But the strain ranges differ greatly on the surface of SU-8, ranging from 3.7×10^{-3} to 6.4×10^{-3} while exhibiting very sharp peaks for the ideal bonding case. However, in the weak bonding case, the strain ranges from 3.8×10^{-3} to 4.1×10^{-3} while exhibiting blunt peaks This is reasonable since the surface of the SU-8 pattern has more constraints on the two sides from the silicon strips while under thermo-mechanical loading, and therefore has a steeper strain gradient cross the SU-8 surface along with a sharp strain jump on the edges for the ideal bonding case.

2.5.5 Measurement results

By spatially scanning the surface of grating with a small spot-size laser, the variation of grating wavelength is captured by the camera as a shift in the diffraction peak position, which can be translated back into strain information through data processing. In this way, one can map the strain distribution on the specimen through measuring the variation of grating wavelength. If a specimen is a single homogenous material, the grating wavelength would be uniform and constant across the sample and increases uniformly with an elevated temperature change. However, for a composite specimen of dissimilar materials the CTE mismatch leads to uneven expansions between different components and thus generates varying grating wavelengths across the surface.

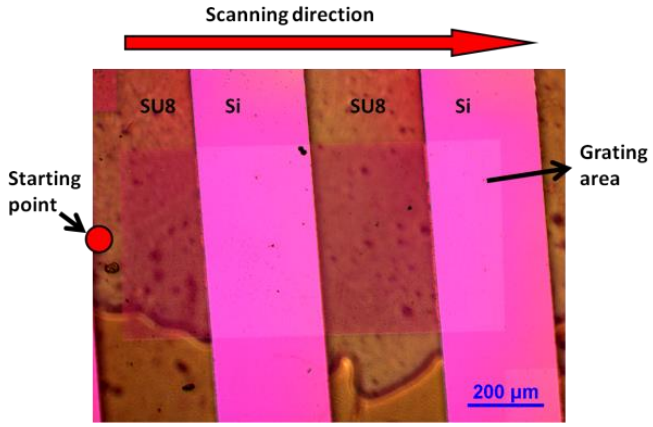

(a)

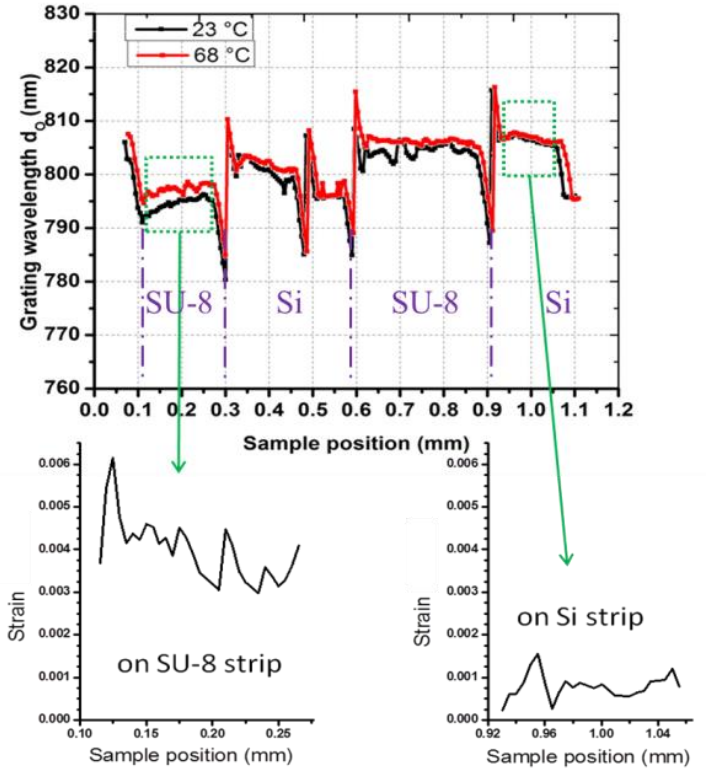

(b)

Figure 2.15. (a) Optical image of a zero thickness grating on a SU-8/Si specimen with the laser scanning area and direction marked. (b) Experimental results of strain sensing. The upper plot shows grating wavelength versus sample position. The laser scans at 23 ˚C (black) and 68˚C (red), respectively. The two lower plots show thermal strains deduced from ΔT=45 ˚C for SU-8 strip (L) and silicon strip (R).

Figure 2.15(a) shows a zero-thickness grating with 800-nm-wavelength fabricated on a SU-8/Si composite specimen using EBL and metal lift-off process. The grating is composed of 50 nm thick parallel gold bars and covers four different SU-8 and silicon zones at an area of 1 mm by 0.5 mm. A laser beam is applied to scan across the surface of the grating in a direction perpendicular to the gold bars at 23 ˚C and 68 ˚C respectively as shown in Figure 2.15(a). The upper plot in Figure 2.15(b) shows the measured grating wavelength versus the scanning horizontal distance on the surface of the grating. It can be seen that at 23 ˚C (room temperature) the grating wavelengths appear four-staged black curve instead of a constant 800-nm-flat-line across the four SU-8 and Si zones. This suggests that the wavelengths of grating at the four zones are not equal and this might be due partially to the metal lift-off step in Acetone that distorts and warps the 300-μm-thick sample. Within each of the four zones the black curve is fluctuate slightly except for one sharp jump in the middle of the left silicon zone probably as a result of the presence of cracks or warpage in Si ribbon. The red curve in the upper plot in Figure 2.15 (b) shows the measured wavelengths as a function of sample position at 68 ˚C. It is noticed that the red curve has upward shifts from the black curve cross over four zones indicating the thermal expansion induced by a temperature change of 45˚C but the two SU-8 regions expands more, which is consistent with the FEA simulation. The strain distributions in the left SU-8 and right Si zones are plotted as shown in the two lower plots in Figure 2.15(b). From left to right on the SU-8 strip, the strain varies between $3 \times 10^{-3} \sim 6 \times 10^{-3}$. On the Si strip, the strain variation is between 6×10^{-4} and 1×10^{-3}. The spatial resolution is around 20 μm, which is defined as the smallest feature size one can detect.

Table 2.1 Strain ranges at SU-8 and Si regions from simulation and measurement.

	SU-8	**Si**
FEA (ideal bonding)	$3.7\times10^{-3} - 6.4\times10^{-3}$	$1.3\times10^{-4} - 2.9\times10^{-4}$
FEA (weak bonding)	$3.8\times10^{-3} - 4.1\times10^{-3}$	$8\times10^{-6} - 2.3\times10^{-4}$
Measurement	$3\times10^{-3} - 6\times10^{-3}$	$6\times10^{-4} - 1\times10^{-3}$

The experimental results from SU-8 region are slightly smaller than the FEA predictions while the experimental results from Si region are larger than the simulation as shown in Table 2.1. Strain distribution analysis isn't performed on the middle region. This is because the strain information in these regions is dominant by other effects, such as warping and imperfections on the grating patterns. Although these factors may impact the regions where analysis is done, they are minor effect compared to the effects discussed in the FEA work.

2.6 Summary

PDMS tunable gratings fabricated through buckled film were used for micro-strain measurement of various materials. A highly sensitive optical setup optimized to amplify a small strain signal to a change in diffraction angle, orders of magnitude larger, was proposed. The applicability of the PDMS/Au grating to infer the strain of the underlying specimen of interest, require the L/h aspect ratio of the grating to greater than 20 for most practical purposes. The thermal strain measurement on the free-standing PDMS grating as well as the PDMS grating bonded to copper and silicon substrates agree well with their reference CTE values. This technique is relatively simple for very high

strain sensitivity measurement, and its potential spatial scanning capability is also expected to complement the application boundaries of other in-plane strain measurement metrologies such as Moiré interferometry or DIC methods in terms of maximum strain gradient, and field-of-view of measurement. In addition, unlike conventional in-plane strain sensing metrologies, the proposed technique is expected to work for non-planar surface geometry, as well.

The laser scanning technique is demonstrated to have both high strain sensitivity and high spatial resolution on pre-defined samples. Note that this technique is capable of detecting localized strain, unlike Moiré techniques (which relies on a sufficient field of view to form Moiré pattern). The CTE measurement for silicon proves the detectable strain to be as small as 10^{-5}. Even though the entire elevated temperature range is only 30˚C, it indicates the capability for monitoring small CTE materials such as Si. This has many applications in different packaging processes, such as reflow, which typically occurs at over 200˚C. Scanning the EBL defined pattern validates the resolvable feature size to be as small as 20 μm. In addition, this technique in principle is able to scan an unlimited field of view, which is determined by the traveling distance of the translation stage. The investigation of strain distribution on the composite sample under thermal loading validates the feasibility of applying this technique towards electronic packages. Future work includes plans for optimizing the system for advancing the strain mapping capability as well as to test this technique on electronic packages.

CHAPTER 3

Buckle ZnO nanoribbons onto soft substrates for stretchable energy harvester[†]

Three pre-patterned ZnO nanoribbons in different configurations were studied in this chapter, including (a) straight ZnO nanoribbons uniformly bonded on soft substrates that form sinusoidal buckles, (b) straight ZnO nanoribbons selectively bonded on soft substrates that form pop-up buckles, and (c) serpentine ZnO nanoribbons bonded on soft substrates via anchors. The nonlinear dynamics and random analysis were conducted to obtain the fundamental frequencies and to evaluate their performance in energy harvesting applications. We found that pop-up buckles and overhanging serpentine structures are suitable for audio frequency energy harvesting applications. Remarkably, almost unchanged fundamental natural frequency upon strain is achieved by properly patterning ZnO nanoribbons, which initiates a new and exciting direction of stretchable energy harvesting using nano-scale materials in audio frequency range.

[†] Based on Teng Ma, Yong Wang, Rui Tang, Hongyu Yu, and Hanqing Jiang. "Pre-patterned ZnO nanoribbons on soft substrates for stretchable energy harvesting applications." Journal of Applied Physics 113.20 (2013): 204503.

3.1 Introduction

Piezoelectric materials, such as lead zirconate titanate (PZT) [70-73], barium titanate ($BaTiO_3$) [74, 75], aluminum nitride (AlN) [76], zinc oxide (ZnO) [77-80], have been utilized to convert mechanical vibration energy into electrical energy for portable or self-powered electronics, among many other application, such as solar cells [81, 82]. Specifically, "piezoelectric nanogenerator" [77], first introduced in 2006, has boomed the applications of nano-scale piezoelectric materials for energy harvesting. One representative configuration of these piezoelectric nanogenerators is a nano-scale piezoelectric cantilever and the energy of mechanical vibration to be harvested is in the vicinity of the system fundamental frequency, which is usually in the high frequency domain for nano-scale materials [83]. In order to accommodate the development of consumer electronics, piezoelectric nanogenerators are expected to be able to integrate with wearable or stretchable devices and different approaches with success to some extent, such as limited stretchability, have been attempted [71, 72, 74, 76, 77]. The deformability, i.e., bendability and stretchability, is realized by bonding buckled piezoelectric materials on top of soft materials. There are two limitations among existing work, namely, energy harvesting only at the high frequency domain, and limited stretchability. To address the limitation of energy harvesting near the fundamental frequency, nonlinear energy harvesting has been explored to achieve large response bandwidth by various approaches [84-89].

Here, we report an approach to utilize pre-patterned ZnO nanoribbons on soft substrates to achieve buckled forms for stretchable energy harvesting applications within audio frequency range. Three pre-patterned ZnO nanoribbons in different configurations

were studied in this chapter, including (a) straight ZnO nanoribbons uniformly bonded on soft substrates that form sinusoidal buckles, (b) straight ZnO nanoribbons selectively bonded on soft substrates that forms pop-up buckles [90], and (c) serpentine ZnO nanoribbons bonded on soft substrates via anchors. These pre-patterned ZnO nanoribbons were first fabricated on silicon-on-insulator (SOI) wafers using dry etching and then brought and bonded with soft materials through transfer printing. The nonlinear dynamics and random analysis were conducted to obtain the fundamental natural frequencies and to evaluate their performance in energy harvesting applications. Remarkably, almost unchanged fundamental natural frequency upon strain is achieved by properly patterning ZnO nanoribbons, which initiates a new and exciting direction of stretchable energy harvesting using nano-scale materials in audio frequency range.

3.2 Experimental

3.2.1 Fabrication of ZnO ribbons free-stood on host substrate

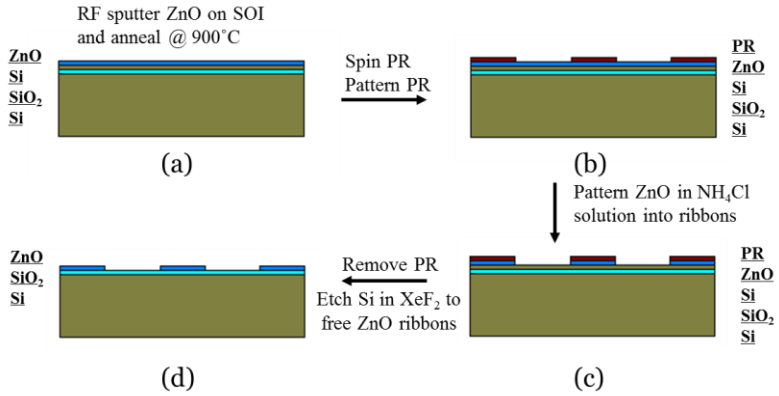

Figure 3.1. Fabrication procedure of ZnO ribbons on SOI wafer.

Figure 3.1 illustrates the fabrication of ZnO ribbons on host substrate, which consists of the following key steps: (1) Preparation of ZnO ribbons on SOI wafers and post-annealing to good crystalline structure. A 370 nm thick ZnO film was deposited on a SOI wafer by RF sputtering with argon-oxygen (50/50) flow at power of 400 W and was annealed at 900˚C to enhance the piezoelectric property (Figure 3.1(a)). (2) Patterning ZnO film into ribbons. Lithography process was performed and ZnO film was wet-etched in ammonium chloride (NH_4Cl) solution (20% by wt) for 10min into ribbons pattern (Figure 3.1(b) (c)). (3) Etching of the silicon sacrificial layer to free the ZnO ribbons from their host. A xenon difluoride (XeF_2) vapor etching (Model: Xetch E1, Xactic Inc.) is performed to remove underlayer silicon without attacking ZnO (etching pressure: 3000mTorr, etching duration time per cycle: 60 s). The exposed silicon between the ZnO ribbons provides an avenue for the XeF_2 gas to undercut and loosen the ribbons without completely dislocating them (Figure 3.1(d)). Photoresist was stripped in acetone after silicon undercutting etching. ZnO ribbons were freed from their host substrate and resting on SiO_2 layer without chemical bonding between them and were ready for the subsequent transfer.

3.2.2 Fabrication of buckling of ZnO ribbons on PDMS

PDMS was prepared by mixing silicone elastomer base and curing agent (Sylgard 184, Dow Corning) at the ratio of 10:1 by weight, pouring into a petri dish, and baking at 80 ˚C for 3 hrs. Rectangular slabs of 1.5 cm by 6 cm were cut from the polymerized piece. Rinse the slab with isopropyl alcohol (IPA) to remove contaminations and dry it using a N_2 gun. A custom made stage was utilized to stretch the PDMS to specific strain levels.

The pre-strained PDMS substrate was subjected to a flood exposure by a UV light (low pressure mercury lamp, BHK), which produces 185 nm and 254 nm radiations, for 150 seconds. The 185 nm radiations produce ozone, while the 254 nm radiations dissociate the ozone to O_2 and atomic oxygen (O) to form a chemically activated surface.

To enhance the interfacial bonding between ZnO and the receiver PDMS, the surface of receiver PDMS was treated by ultraviolet (UV) to form hydrophilic surface (terminated with $-O_nSi(OH)_{4-n}$ functionalities), which is able to form strong chemical bonding through condensation reactions with various inorganic surfaces that have -OH groups (such as the surface of ZnO in the ambient environment) [91, 92].

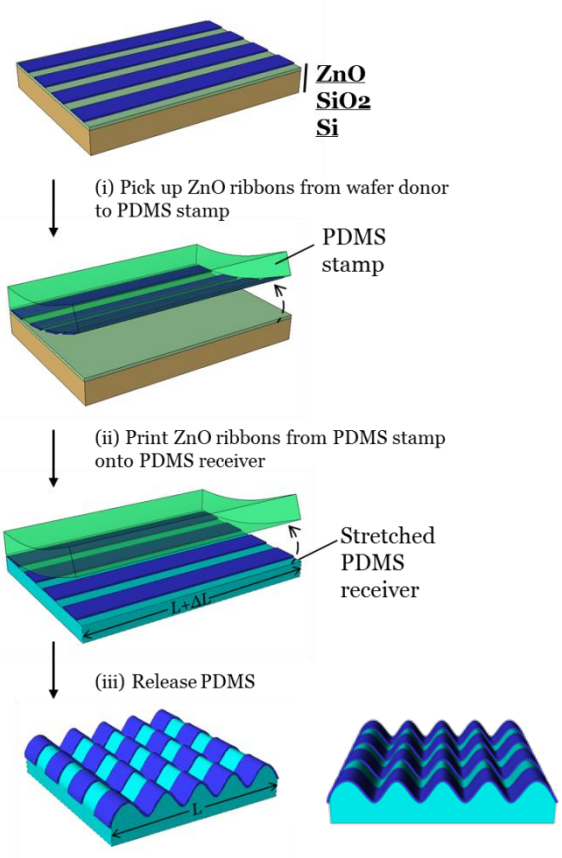

Figure 3.2. Fabrication procedure of buckling ZnO ribbons on PDMS

Figure 3.2 illustrates the transfer printing approach of buckling ZnO on PDMS. ZnO ribbons (tens of micron wide and 370 nm thick) were patterned on a SOI host substrate as described previously and subsequently released from the mother substrate using XeF_2 silicon etching. A piece of PDMS (thickness 8-12 mm) as a stamp was bringing into conformal contact with the wafer and quickly peeling it back to retrieve the ordered ZnO ribbon arrays. ZnO ribbons were retrieved from the host substrate by the PDMS stamp via adhesive van der Waals forces in the surface-dominated ribbons. Next, a second slab of PDMS (~2mm thick) as receiver substrate was elastically stretched by 5% prestrain and exposed to UV light for 2min for surface modification. After that the PDMS substrate then was brought into conformal contact with the PDMS stamp. Peeling off the PDMS stamp allowed for complete transfer of the ZnO ribbons to the PDMS substrate via covalent interfacial force. Finally, releasing the prestrain in the PDMS substrate led to a compressive force in the ZnO ribbons as the PDMS relaxed to zero strain, leading to surface deformations and buckling in both ZnO ribbons and the PDMS surface and resulting in a flexible ZnO rubber. The resulting wavy geometry is a result of the transfer of mechanical compressive energy into bending energy.

3.2.3. Fabrication of controlled buckling of ZnO ribbons on PDMS

Previously described buckling of ZnO ribbons is highly stretchable but also has its limitations. The entire PDMS surface is treated by UV/ozone exposure or by oxygen plasma and the buckling occurs in both ZnO ribbons and the upper surface of PDMS as well due to the strong bonding between them. The spontaneously formed wavy structure has fixed period and amplitudes depending on the ribbon thickness, prestrain and the

mechanical properties of both ZnO and PDMS. This wavy structure is typically called small wave with typical period in the range of only tens of micron which can accommodate maximum strains no more than 30%. Here we use a UVO mask technique [43, 93] to selectively treat PDMS surface to achieve buckling configurations with much wider buckling period which enables extreme stretchability of the buckled ZnO ribbons.

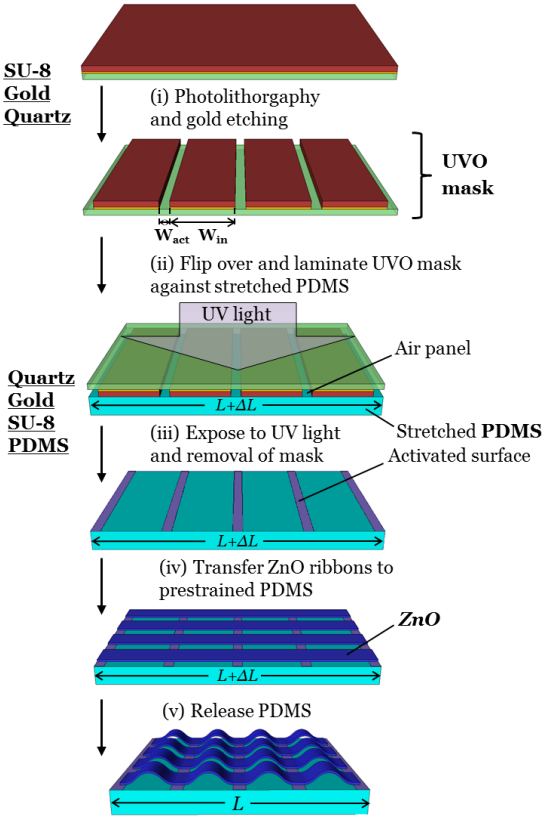

Figure 3.3. Process steps of a UVO mask and controlled buckling of ZnO ribbons [43, 93]

Figure 3.3 illustrates the fabrication of a UVO mask, its use in selectively treating PDMS and generating controlled ZnO ribbon buckling. Quartz slides coated with titanium (Ti), gold (Au), and photoresist were used as UVO masks. Before metal deposition, quartz slides were dipped in to freshly prepared piranha solution (3:1 H_2SO_4/30%H_2O_2) for 1 h to remove organic impurities. After rinsing in deionized water

and drying with a N_2 gun, cleaned slides were coated with 5 nm Ti and then 100 nm Au by E-beam evaporator at ultra-high vacuum (UHV). Ti was used as adhesion layer for Au and Au was employed as the mask layer for UV light. Negative photoresist SU-8 2015 (MicroChem) was spin-coated on the slides for 30 s at 4000 rpm to obtain a 13 μm-thick thin film. Standard lithography process was then performed to pattern SU-8 2015 and residue photoresist was then removed in an oxygen plasma asher leaving the desired photoresist pattern as hard mask for final Ti/Au etching. The exposed Au and Ti area were etched in gold etchant (TFA) for 1 min and titanium etchant (1:1:20 $HF/H_2O_2/H_2O$) for 30 s, sequentially.

A pre-stretched PDMS substrate was exposed to UV light through the UVO mask to pattern the surface chemistry, namely activated area in width W_{act} for strong bonding and inactivated area in width W_{in} for weak bonding. Using the previous transfer printing approach, ZnO ribbons were transferred to the pre-stretched and chemically patterned PDMS. The relaxation of the pre-strain on the PDMS led the ZnO ribbons on inactivated areas to delaminate from PDMS and form the periodic pop-up buckles anchored on activated areas (Figure 3.1(f)). The patterns of pop-up buckles (referred as big waves thereafter) can be precisely controlled by the UVO mask with considerable wavelengths.

3.2.4 Fabrication of hanging-over ZnO serpentine on PDMS

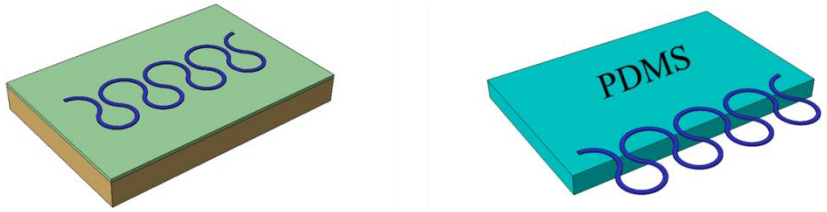

(a) (b)

Figure 3.4. Fabrication process of ZnO serpentine hanging over PDMS (a) Serpentine ZnO nanoribbons rest on SOI wafer after the top silicon layer is etched away. (b) Serpentine ZnO nanoribbons are transferred to a PDMS substrate with one side hanging over. This configuration is referred as hanging-over serpentine.

We can also fabricate ZnO serpentine structure hanging over the edge of PDMS using the previous process approach. The serpentine ZnO nanoribbons resting on the SOI wafer (Figure 3.4(a)) were finally transferred to a receiver PDMS substrate anchored at one side to form a hanging-over serpentine structure (Figure 3.4(b)).

3.3 Experimental results

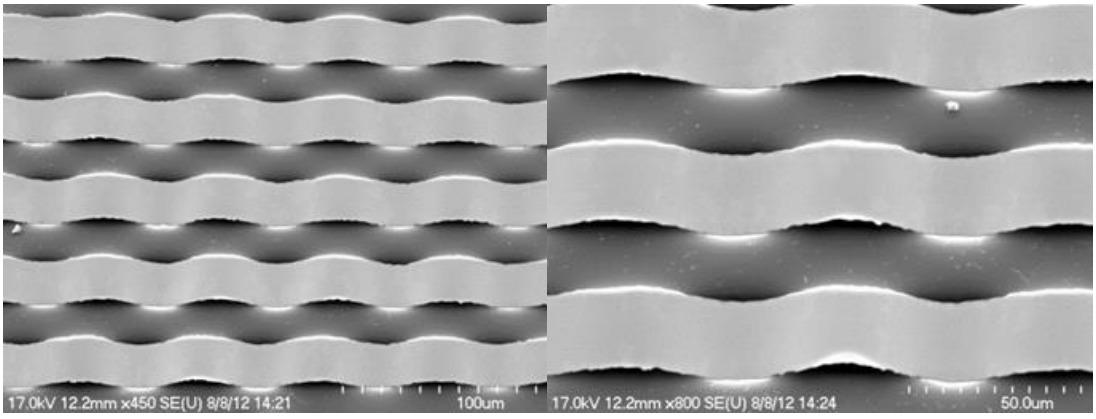

Figure 3.5. SEM images of buckled ZnO ribbons on PDMS. The pre-strain is 5% and the buckling wavelength is 60.2 μm.

Figure 3.5 shows titled-view SEM images of the small waves ZnO ribbons on PDMS with 5% pre-strain. The wavelength was measured as $\lambda = 60.2\mu m$, which can be

captured by the theoretical analysis [42] that gives buckling wavelength as $\lambda = 2\pi h_{ZnO}\left[E_{ZnO}\left(1-\nu_{PDMS}^2\right)/3E_{PDMS}\left(1-\nu_{ZnO}^2\right)\right]^{1/3}$, where h is the thickness, E is the Young's modulus; ν is the Poisson's ratio, and the subscripts refer to ZnO nanoribbons and PDMS substrate. When the following literature values for the mechanical properties (E_{ZnO} = 129GPa, ν_{ZnO} = 0.349, E_{PDMS} = 2MPa, ν_{PDMS} = 0.48) are used [94, 95], the theoretical solution gives $\lambda = 61.8\mu m$, which agrees very well with experiments without any parameter fitting.

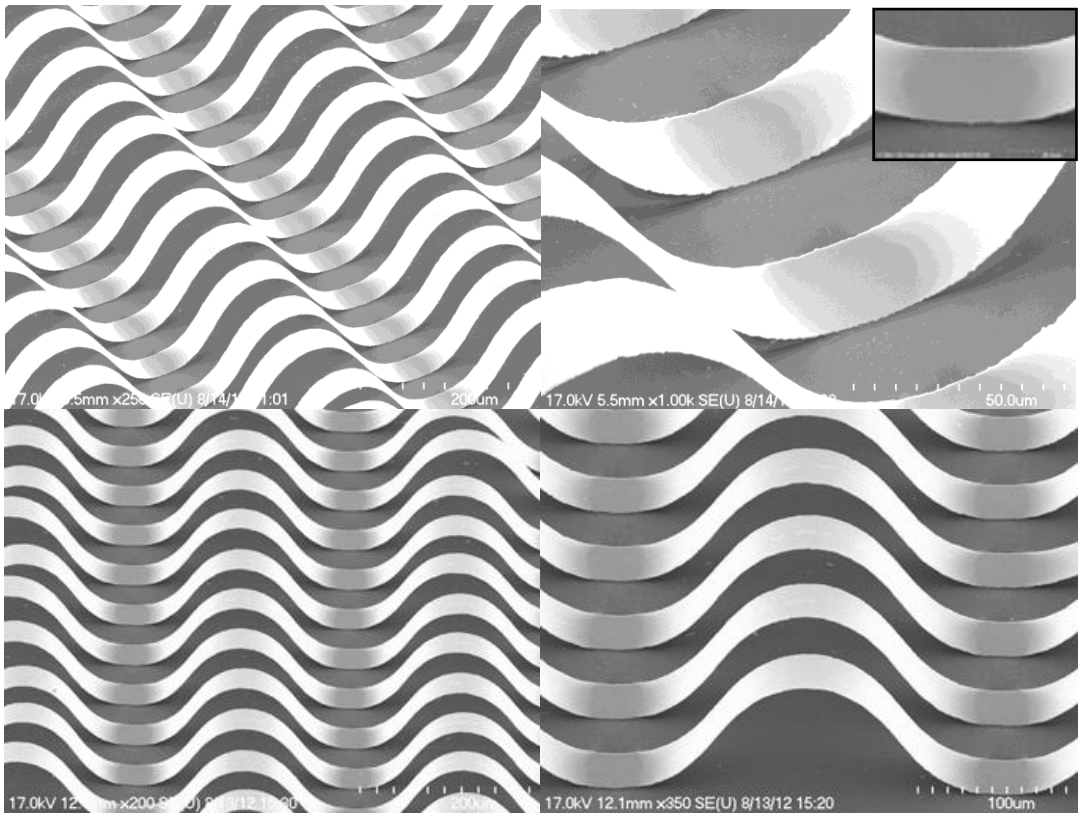

Figure 3.6. SEM images of controlled buckling of ZnO ribbons with W_{act} = 20 μm, W_{in} = 480 μm and ε_{pre} = 60%. The buckling wavelength is 292 μm.

Figure 3.5 shows SEM images of big waves with W_{act} = 20μm, W_{in} = 480μm, and ε_{pre} = 60 %. The buckling wavelength was measured as 292μm, which also agrees well with the theoretical analysis [96] $\lambda = W_{in}/(1+\varepsilon_{pre}) = 300\mu m$.

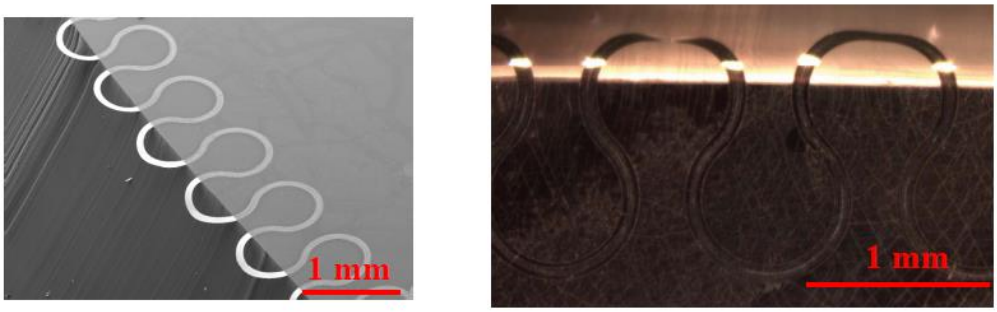

(a) (b)

Figure 3.7. (a) SEM image of a hanging-over serpentine ZnO nanoribbon. (d) Optical image showing a hanging-over serpentine subject to 30% applied strain, where the twisting at the overhanging segment is observed. The width of serpentine ribbon is 100 μm.

Figure 3.6(a) shows the hanging-over serpentine ZnO nanoribbons on the edge of PDMS substrate. The width of serpentine ribbon is 100 μm. Figure 3.6(b) shows an optical image of a hanging-over serpentine ZnO ribbon subject to 30% stretching, where the twisting is observed.

These three configurations of patterned ZnO nanoribbons all present excellent stretchability. The small waves and big waves are stretchable through the change of buckling profiles. For example, upon tension the buckling wavelength increases and amplitude decreases in a similar way as an accordion bellow. The big wave can be stretched up to the level of the pre-strain, such as 60% in Figure 3.5. The stretchability of the hanging-over serpentine ZnO nanoribbons is through the twisting of the hanging-over segment, which is similar to stretching the coiled telephone cord.

3.4 Discussions

The dynamic properties of these three configurations of pre-patterned ZnO nanoribbons are theoretically examined for energy harvesting applications. As the small waves are firmly bonded on PDMS, any mechanical vibrations on ZnO nanoribbons are damped by PDMS, which dissipates the vibration energy stored in ZnO nanoribbons rapidly. Thus, the small wave structure is not suitable for energy harvesting application though there are some efforts to utilize this structure as a platform to develop stretchable energy harvesting devices but no meaningful experimental measurements exist for harvested energy yet.

For big waves, the dynamic analysis [97] has found that the fundamental natural frequency $\Omega/\left(\sqrt{E_{ZnO}/(12\rho_{ZnO})}h_{ZnO}/W_{in}^2\right)$ does not depend on the level of strain and remains a constant (7.06) as long as $\left(\varepsilon_{pre}-\varepsilon_{applied}\right)/\left[\left(1+\varepsilon_{pre}\right)\varepsilon_{cr}\right]>3.4$, where Ω is the fundamental natural frequency, ρ = 5,610kg/m^3 is the density of ZnO, $\varepsilon_{applied}$ is the applied strain on the buckled structure, $\varepsilon_{cr}=\left(\pi h_{Zno}/W_{in}\right)^2/3$ is the critical strain for pop-up buckling [90]. For nanoribbons (i.e., h_{ZnO}/W_{in} is on the order of 10^{-4}), ε_{pre} is much greater than ε_{cr} so that the criterion $\left(\varepsilon_{pre}-\varepsilon_{applied}\right)/\left[\left(1+\varepsilon_{pre}\right)\varepsilon_{cr}\right]>3.4$ for strain-independent fundamental natural frequency holds as long as $\varepsilon_{applied}$ does not reach ε_{pre}. Though the analysis is for small deformation but the strain-independence of natural frequency to strain has been validated through finite element simulations. This relation is critical to develop stretchable energy harvesting devices, as upon deformation, the frequency range harvested by the structure does not prominently vary. The fundamental

natural frequency is very important to energy harvesting and always designed to match the environmental frequency through the selection of geometric dimension of the structure. Due to the invariance of the fundamental natural frequency to pre-strain, the length and thickness of the ZnO nanoribbons can be designed through the equation $\Omega / \left(\sqrt{E_{ZnO} / (12\rho ZnO)} h_{ZnO} / W_{in}^2 \right) = 7.06$ for given fundamental natural frequency Ω, elastic modulus E and density ρ of ZnO. Figure 3.7(a) provides a phase diagram of the natural frequency Ω as a function of h_{ZnO} and W_{in}. We are particularly interested in letting the natural frequency fall into the range of audio frequency (20 to 20,000 Hz), since the audio frequency exists everywhere in the ambient environment and provides a wide range to harness the vibration energy from the environment. The natural frequency of the big wave with $h_{ZnO} = 370nm$ and $W_{in} = 480\mu m$ shown in Figure 3.5 falls into range of audio frequency.

Another important factor in energy harvesting is that the external vibration sources have a wide spectrum of frequencies [89], such as 20 to 20,000 Hz for audio frequency. The random analysis was conducted for big waves to determine the dynamic response under random excitation. The external random vibration sources alter the buckling profiles and the associated bending energy, which can be converted to electrical energy. Thus, the expectation of the change of bending curvature under random excitation provides a means to find out the location of maximum harvestable bending energy, which is practically important for the energy harvesting devices. Figure 3.7(b) shows the distribution of normalized mean-square value of bending curvature change $E\left[v''^2 \right]$ upon random excitation for different damping μ, along the ribbon direction.

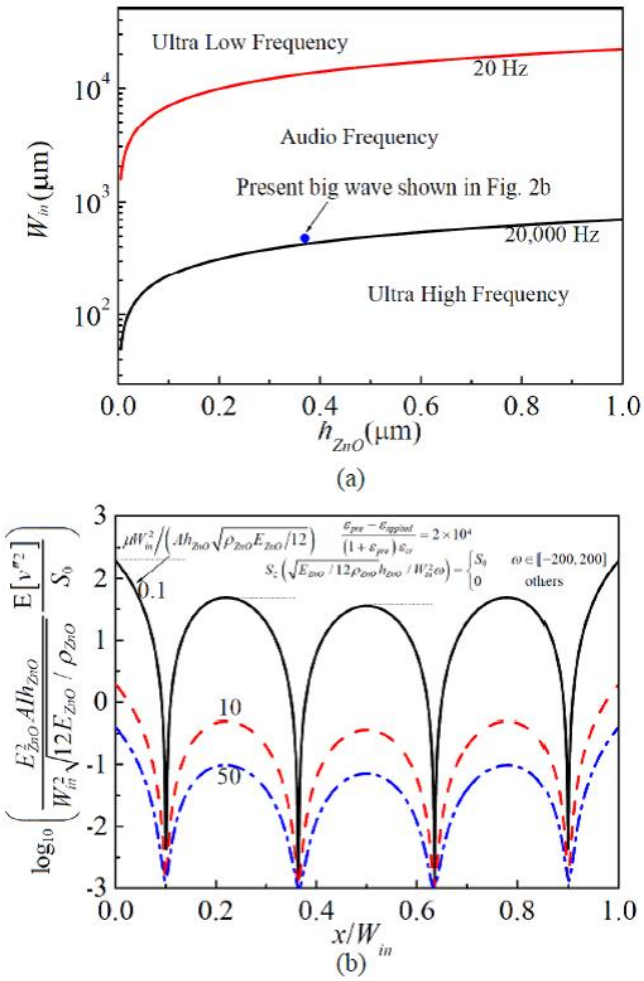

Figure. 3.8. Theoretical analysis of the dynamic behavior of big waves. (a) Phase diagram of the fundamental natural frequency of big waves by choosing the thickness of the nanoribbons (h_{ZnO}) and the patterning of the PDMS substrates (W_{in}). Three distinct frequency domains are shown, namely ultra-low frequency, audio frequency, and ultra-high frequency. The big waves in FIG. 2b fall into the audio frequency domain. *A* is the cross-sectional area and *I* is the moment of inertia. (b) The mean-square value of bending curvature change $E\left[v''^2\right]$ upon random excitations, normalized by the strength of the power spectrum density S_0 of the random excitation, as a function of normalized location x/W_{in} for different damping factor μ. Here the power density spectrum $S_\xi(\omega)$ of the random excitation is taken as constant S_0 at $\omega \in [-200, 200]$ and 0 otherwise; the strain is taken as $(\varepsilon_{pre} - \varepsilon_{applied}) / [(1+\varepsilon_{pre})\varepsilon_{cr}] = 2\times10^4$, where $\varepsilon_{applied}$ is the applied strain on the big waves and $\varepsilon_{cr} = (\pi h_{Zno} / W_{in})^2 / 3$ is the critical strain for big waves.

It is found that the maximal mean-square value of bending curvature change appears at $x/W_{in}=0$ and 1, which corresponds to the anchor points between the activated and inactivated areas. Other extreme values appear at $x/W_{in}\approx 1/4$, 1/2 and 3/4 and the expectation at $x/W_{in}\approx 1/4$ and 3/4 is larger than that at $x/W_{in}\approx 1/2$. In energy harvest application, to reach large energy output, the electrodes should be placed at the locations with maximal mean-square value of bending curvature change, or equivalently, the maximal harvestable bending energy. Figure 3.7(b) actually suggests the optimal locations of the electrode at $x/W_{in}=0$ and 1 and then $x/W_{in}\approx 1/4$ and 3/4.

For serpentine structures without displacement loading, the fundamental natural frequency was estimated by using the beam theory and given by $\Omega = 0.56 h_{ZnO}\sqrt{E_{ZnO}/12\rho_{ZnO}}/l_{eff}^2$, where l_{eff} is the equivalent length of the serpentine structure and is selected as the length of the cantilever part. For structure shown in Figure 3.6, the length of the cantilever part, or the equivalent length $l_{eff}=345\mu\text{m}$, the natural frequency is approximately 2,407.7 Hz, which is in the audio frequency range. This indicates that the serpentine structure is capable to harvest the vibration energy in the ambient environment, which is in audio frequency range. The finite element simulations were also conducted to study the relationship between frequency and applied strain. Figure 3.8 shows the fundamental frequency as a function of applied strain. It is found that at vanishing applied strain, the fundamental natural frequency is 1,472.8 Hz, on the same order of that obtained from the approximated beam theory. As strain increases, the natural frequency varies steadily but remains at the audio frequency range even at the 15% applied strain. With increase of the length of the cantilever part, the frequency has less

dependence on the applied strain. Again interestingly, the over-hanging serpentine structure provides another design of reaching audio and strain insensitive frequency for harvesting ambient energy in audio frequency range.

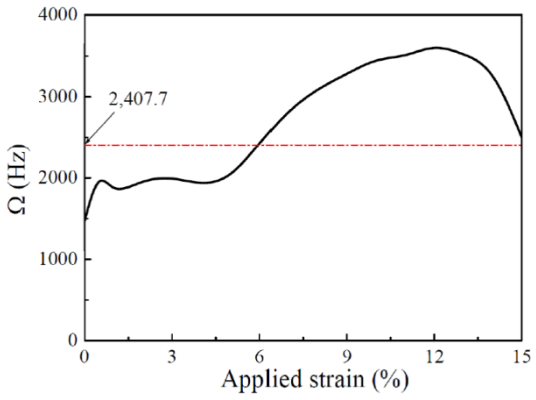

Figure. 3.9. Theoretical analysis of the dynamic behavior of hanging-over serpentine ZnO nanoribbons. Finite element simulation results are shown as the plot of fundamental natural frequency Ω as a function of applied strain. It is found that the fundamental natural frequency remains in the audio frequency domain and does not strongly depend on applied strain.

3.5 Summary

Three forms of ZnO nanoribbonson PDMS substrates were fabricated through lithography patterning, namely small waves, big waves and overhanging serpentine structure, and their applications on stretchable energy harvesting applications were discussed through theoretical analysis. It was found that big wave and overhanging serpentine structures show strain-insensitive fundamental natural frequencies in the audio frequency range upon applied strain, which provides a means to develop stretchable energy harvesting devices for various applications. Though the demonstration in this chapter is for ZnO, the methodology can be applied to other piezoelectric materials, such as PZT with much stronger electrical-mechanical coupling. We expect that this work is

able to enlighten a broad field of stretchable energy harvesting devices within audio frequency range. We also notice that the analysis in this chapter does not consider multilayer structures that are employed in the real devices, though the similar analysis can be conducted by using the effective material properties of the multilayer structures.

CHAPTER 4

Silicon thin-film on soft substrate as anodes for lithium ion batteries[†]

High energy capacity Li-ion batteries using Si film anodes are found to have a long cyclic life by successful relaxation of the stress induced during lithiation and delithiation. A soft elastomer substrate in the Si-film-anode plays a beneficial role for improved performance of the battery, which suggests a general way to solve the bottleneck problem for Si anodes.

[†] Based on Cunjiang Yu, Xin Li, Teng Ma, Jiepeng Rong, Rongjun Zhang, Joseph Shaffer, Yonghao An, Qiang Liu, Bingqing Wei, and Hanqing Jiang. "Silicon Thin Films as Anodes for High‐Performance Lithium‐Ion Batteries with Effective Stress Relaxation." Advanced Energy Materials 2.1 (2012): 68-73.

4.1 Introduction

There is a great deal of interest in developing next generation lithium ion (Li-ion) batteries with higher energy capacity and longer cycle life for a diverse range of applications such as portable electronic devices, satellites, and the next-generation electric vehicles. Silicon (Si) is an attractive anode material that is being closely scrutinized for use in Li-ion batteries because of its highest-known theoretical charge capacity of 4,200 mAh/g [98]. The development of Si-anode Li-ion batteries has lagged behind, however, mostly because of the large volumetric changes (up to 400%) that occurs upon insertion and extraction of Li ions, and in turn the large electrochemical related stress, which results in electrode pulverization, loss of electrical contact and early capacity fading of battery cells [99-102]. Despite this challenge, the extraordinarily high energy capacity of Si in its own right has motivated researchers to develop new techniques that curb the limitation of Si as a practical anode material. Ultra-thin Si film down to 50 nm has been reported for successful anti-pulverization and capacity non-degradation over two thousand charging/discharging cycles on roughened current collectors [103]. This, together with a surge of work besides that on improving the capacity retention of Si anodes such as: nanoparticles [104, 105] and/or composites [106-109], nanowires [110-112], nanotubes [113, 114], which can offer expansion spaces during lithium insertion/extraction (Figure 4.1(a)) have shown improved performances. However, some extent of capacity fading still exists due to limited space for accommodating the facile strain expansion as well as decreased accessibility of the electrolyte to the solid electrolyte interphase (SEI) between the silicon nanostructures and electrolyte. Here,

we present a new strategy of stress relaxation for Si films using elastomeric substrate that will establish an alternative route for new electrode design. Besides, the design of the anodes offers more efficient ion and electron transportation than those reported work using nanoparticles, nanowires, and nanotubes.

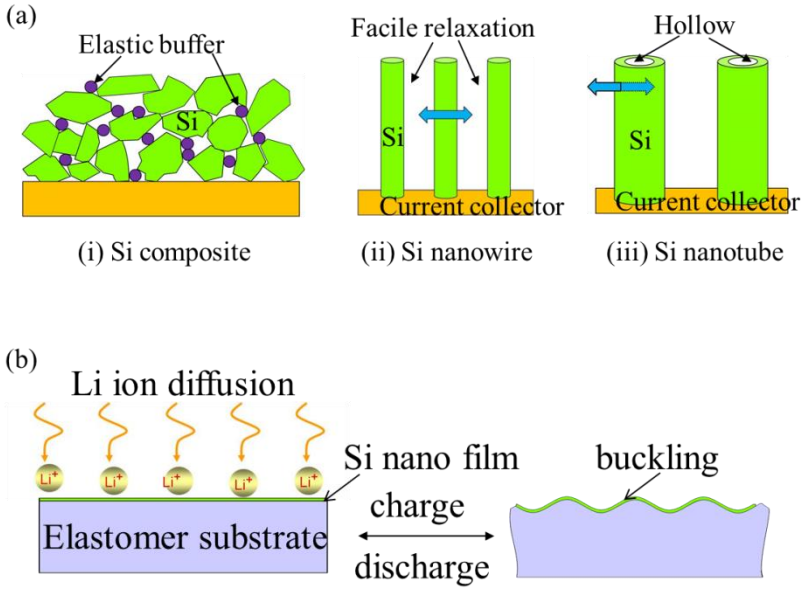

Figure 4.1. Different approaches to achieve longer cyclic life time for Si based anodes of lithium ion batteries. (a) Various nanostructured Si as anodes in Li ion batteries. (i) Si nanocomposites using elastic matrix to act as buffers for the strain release; (ii) Si nanowires and (iii) Si nanotubes utilizing the lateral free surface to accommodate volume expansion. The approach (b) using soft substrates to release the lithiation-induced stress in Si thin film during cyclic charge/discharge. The compressive stress is released by generating out-of-plane deformation, i.e., buckling.

The general concept of stress relaxation can be understood using an eigen strain analogy. It is well-known that the eigen deformation of a free-standing material does not lead to mechanical stress, but only self-compatible deformations, and eigen strain induced stresses are generated when the eigen strain is constrained. Consequently, the stress can be released by removing these constraints (e.g., stainless steel in [110] and rough substrates in [103]). In the following, we report an approach

in which the rigid substrates (e.g., current collectors) that constrain the "free" expansion/contraction of the Si anodes during charge/discharge are replaced by soft substrates. The mechanism for stress relaxation lies in that the volumetric strain in Si induced by charge/discharge cycling can buckle the flat Si thin films on soft substrates (Figure 4.1(b)), in turn releasing the stress in Si films by balancing the electrochemical induced axial component and buckling induced bending component of stress. The similar mechanism has been extensively studied for compressing stiff thin films on elastomeric substrates [15, 42] and successfully utilized to develop stretchable electronics [115, 116], though the mechanism to be presented here is different from that in existing studies. This article presents experimental studies that demonstrate the proof-of-concept and exhibit superb performances of Si film anodes based Li ion batteries resulting from successful stress relaxation. Theoretical examinations including continuum analysis and first-principle calculations provide qualitative understanding of such electrochemical-mechanical coupled system.

4.2 Experimental

The realization of Si anodes involves the fabrication of Si thin films from bulk Si wafer, then separation of these two by undercutting the inter-media layer, and finally transfer printing Si thin films as anodes onto soft substrates. Figure 4.2(a) illustrates the procedure for fabricating the Si anodes. The Si anodes are derived from the device layer of silicon-on-insulator (SOI) wafers (Soitec Inc.), whereas low-cost Si materials from chemical vapor deposition (CVD) are adoptable without adding any complexity following the procedures below with large scale capabilities. PDMS

polymer was used as the soft substrate and its stability in the electrolyte (1 M LiPF6 + EC + DEC (1:1 in volume)) was carefully examined under room temperature within argon ambient, where no mechanical or chemical degradation has been found. The fabrication started from patterning the top Si (100 nm to 400 nm) of SOI wafers into ribbons (75 μm-width) and removing the buried SiO_2 layer (400 nm). Thin layers of chromium (5 nm), gold (100 nm) and chromium (5 nm) were then deposited in sequence on top of the Si ribbons, followed by oxidizing the top Cr layer. A flat PDMS substrate (1-2 mm thick) was brought into contact with the multi-layer structure (Cr_2O_3/Au/Cr/Si). Prior to the contact, the PDMS surface was treated by ultraviolet/ozone (UVO) light, which changed the surface properties of PDMS [91, 92] and helps to form strong chemical bonds via condensation reactions with various other surfaces that have -OH groups, such as the covalent bonds (-Si-O-Cr) between PDMS and Cr_2O_3. Peeling the PDMS away resulted transferred multi-layers onto the PDMS as the formation of the Si anodes on the soft PDMS substrate with the underneath Au current collector, in order to take advantage of the short diffusion distance along the Si thickness direction, which offers more efficient ion and electron transportation than those reported work using nanoparticles, nanowires, and nanotubes, and therefore benefits high-power density. Finally, thin layers of Cr (10 nm) and Au (100 nm) were deposited on top of the two ends of the Si ribbons through a shadow mask as a means of wiring out.

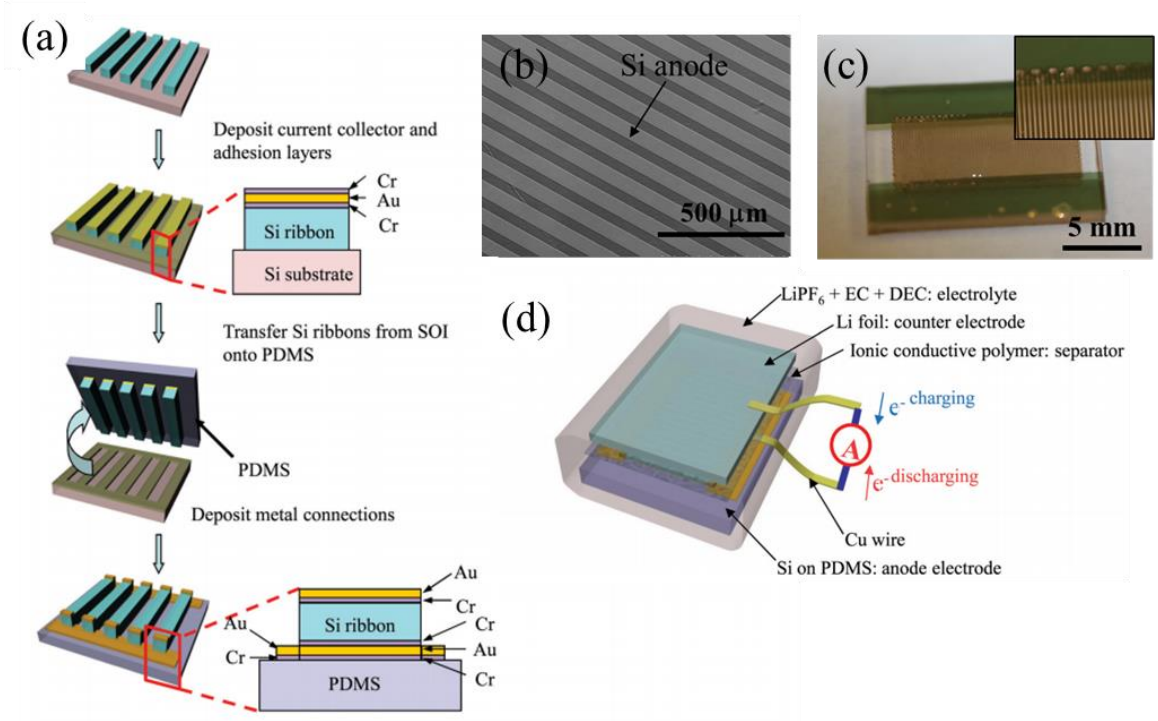

Figure 4. 2. Half-cell lithium ion battery based on Si anodes by microfabrication. (a) schematic steps to fabricate the Si anodes on PDMS substrates. (b) An SEM image of Si anode on PDMS, and (c) optical images of fabricated anode before assembling. (d) An illustration of the battery cell assembly.

Figure 4.2(b, c) show the SEM and optical images of a fabricated Si anode on a PDMS substrate, respectively. Figure 4.2(d) illustrates a schematic assembled testing cell with fabricated Si anode and lithium metal as reference as well as counter electrode. The mass of Si anodes can be precisely determined by the well-defined geometries of the Si ribbons by photolithography and the well-accepted density of Si [117]. The typical mass of Si anodes used in this study varies from 5.8 μg to 16.3 μg for different Si patterns and Si thicknesses.

4.3 Results and discussion

The electrochemical characterizations have been conducted on the assembled HS-test cells (Hohsen Corp.). Here the surface of the Si anodes has not been particularly modified so that the SEI is similar to other reported work. Figure 3A is a striking example of the long cyclic stability of a half-cell battery up to 500 cycles with nearly 85% capacity retention. The cell was galvanostatically charged and discharged within a voltage window of 0.005-3.000 V (vs. Li/Li+) at C/4 rate (the charge/discharge rate was calculated based on the theoretical capacity of 4,200 mAh/g for Si and the C/4 rate corresponds to a current density allowing a full discharge in 4 h). It is noted that the first cycle was not counted because of a varying C rate (0.1 C) and formation of the SEI layer. Compared to specific capacities reported for silicon-based lithium ion batteries [102], the battery from the Si thin film on PDMS substrate features an extremely low fading rate (15.4% over 500 cycles, equivalent to 0.033% degradation per cycle at C/4 rate) and a high specific capacity (up to 4,137 mAh/g at the beginning and at 3,498 mAh/g at the 500th cycle), indicating much improved cycling stability compared to conventional Si electrodes, which usually fade quickly after tens of cycles due to the well-known volumetric change during Li ion insertion and extraction (for instance, a pure Si anode degraded from ~3,200 mAh/g to ~300 mAh/g after 20 cycles, equivalent to 4.5% degradation per cycle [118]). To be noted that the strategy of stress relaxation provides significant tolerance to Si thickness (up to 400 nm for the present study though by no means of optimazation) compared to the previous study, where the thickness of the Si anode was limited to 50 nm and the surface of the current collector needs to be roughened [103]. Although theoretical

studies [119-122] predict that ultra-thin films or tiny particles, together with plastic deformation and slow charging rate would somehow avoid fracture, alternatively, stress relaxation would have profound significance to meet the requirements of current batteries with thicker anodes and/or cathodes.

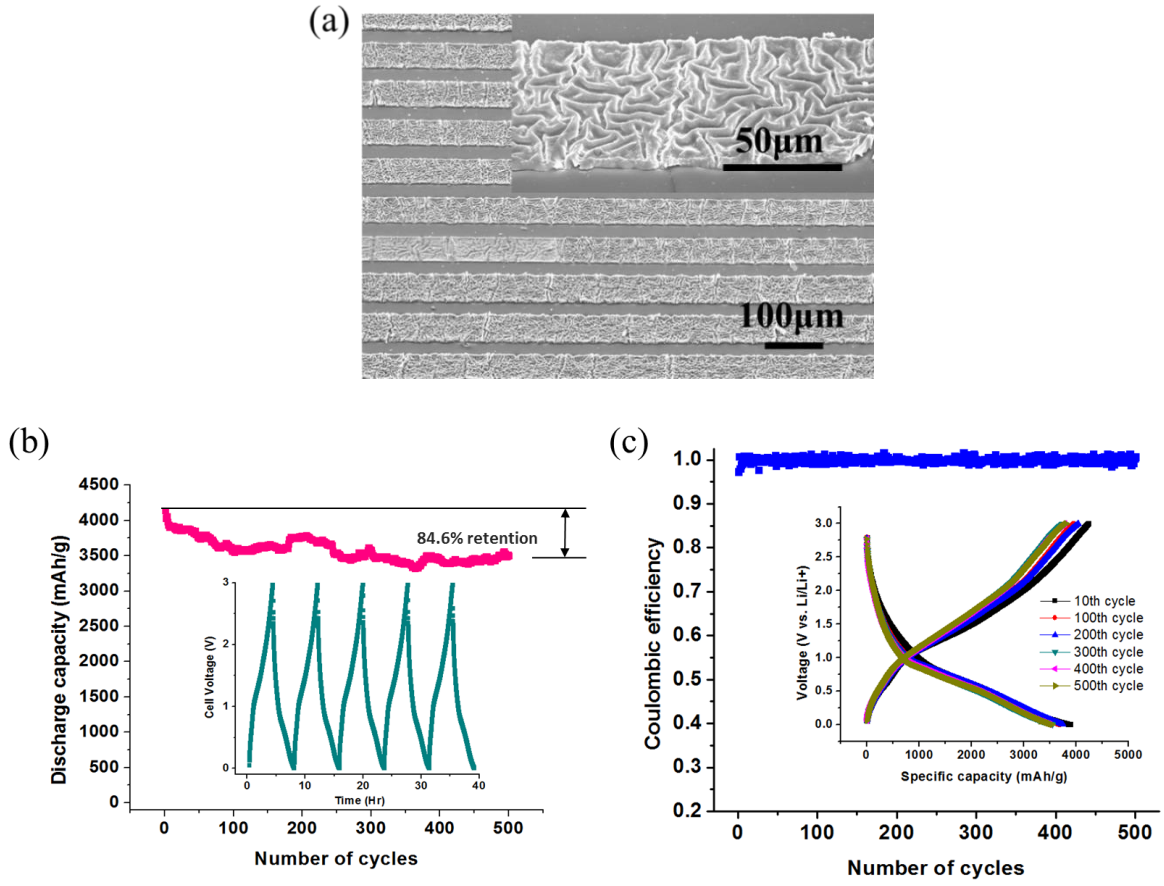

Figure 4.3. Electrochemical testing of Si anodes based lithium ion batteries. (a) SEM images show the buckled Si after lithiation after six cycles charge/discharge under the charge rate of 1C. The insert is an enlarged image clearly shows the buckling morphology. Si ribbons buckle on soft substrates due to electrochemical reactions. (b) Long cycle stability of the battery cell up to the 500th cycle with nearly 85% capacity retention. The inset is a typical charge/discharge profile from the 13th cycle to the 18th cycle). (c) Columbic efficiency from the 1st cycle to the 500th cycle shows high value of 99% to nearly 100% efficiency. The inset includes I-V profiles of the 10th, 100th, 200th, 300th, 400th, and 500th cycles, respectively.

The superb cycle stability is primarily attributed to the unique combination of the Si ribbons and the soft PDMS substrate, which helps to release the lithiation stress in Si via buckling of Si ribbons. The evolution of the morphology change of the Si anodes has been evidenced in situ (see Movie S1 in ref [49]). Figure 4.3(a) shows the SEM images of buckled Si ribbons (400 nm thick and 75 μm wide) after six cycles charge/discharge under the charge rate of 1C, which verifies the hypothesis that the lithiation strain buckles the Si thin films on soft substrates. The buckled structures, similar to springs, accommodate the accumulated stress so as to avoid cracking and crumbling of the Si electrode, thus maintaining the structural integrity and in turn, contributes to the superior cycling performance. We noticed that some cracking or extreme localized wrinkles exist, which may be caused by cell assembling.

Figure 4.3(c) demonstrates a significantly stable and high Colombic efficiency up to 500 cycles. The Colombic efficiency, defined here as the ratio of the capacity of the charge immediately following the previous discharge, is from 92% to 95% throughout the duration of the entire 500 cycles. This data, higher than most of the reported values for Si-based lithium batteries which have lower than 90% of the Colombic efficiency [113, 123, 124], complements the low capacity fading shown in Figure 4.3(b) and indicates that the PDMS substrate plays a tremendously beneficial role in holding the electrode while allowing it to expand and contract reversibly during the repeated lithiation and delithiation processes. The consistent charge-discharge profile (Voltage vs. Specific capacity) demonstrated as the inset of Fig. 3C shows an excellent stability of the dynamic processes during the Li-ion inserting into and extraction out of the Si lattice. Interestingly, the insertion and extraction

processes appear across the entire potential window (0-3.0 V), and this Si anode system has an asymmetric reaction window, mostly below 1.0 V for the insertion process and above 1.0 V for the extraction process, distinguishing it from other Si anodes which have a relatively symmetric reaction window all below 0.5 V [125]. This unique phenomenon cannot be simply interpreted as a pure Li/Si redox reaction and/or nanostructural effect [125]. It is plausible that the stress relaxation from the soft substrate may have different effects on the Li ion insertion and extraction. Since the huge mechanical deformation in Si during electrochemical reactions (e.g., 400% volumetric change), the strain energy (proportional to the square of the deformation) is untypically comparable to the electrochemical energy (hundreds of kJ/mole as a typical scale). Thus, it is very likely that the mechanical deformation (e.g., the stress relaxation in the present work) affects the battery performance and raises new scientific phenomena, such as charge-discharge profile in Figure 4.3(c) and many others [126]. The fundamental understanding of this unique phenomenon is underway.

Figure 4.3(b) contains two pieces exciting information: long-cyclic stability and high specific charge capacity, both are related to stress relaxation. The mechanism of relaxation of the stress associated with the electrochemical reaction can be qualitatively understood using continuum analysis. To simplify the problem, we create a two-dimensional model by considering a Si thin film (100 nm thick) bonded to a relatively thick PDMS substrate (500 μm) and ignoring other components, using the finite element analysis package ABAQUS. The Si thin film is modeled as an elastic-plastic material because plastic flow in Si anodes has been experimentally

identified [127-129]; and the PDMS is modeled as an elastic material. The modeling details can be found in SI section. Because of the buckling, the stress in the Si is non-uniform, i.e., tension and compression on the two sides of a neutral plane. Figure 4 shows the evolution of the maximum Si stress (both tension and compression) with the state of charge (Supplementary Information). It is noticed that the maximum stress at 50% state of charge is only about 500 MPa, much smaller than that of the same Si thin films on a rigid substrate, which shows the relaxation of the stress by using soft materials.

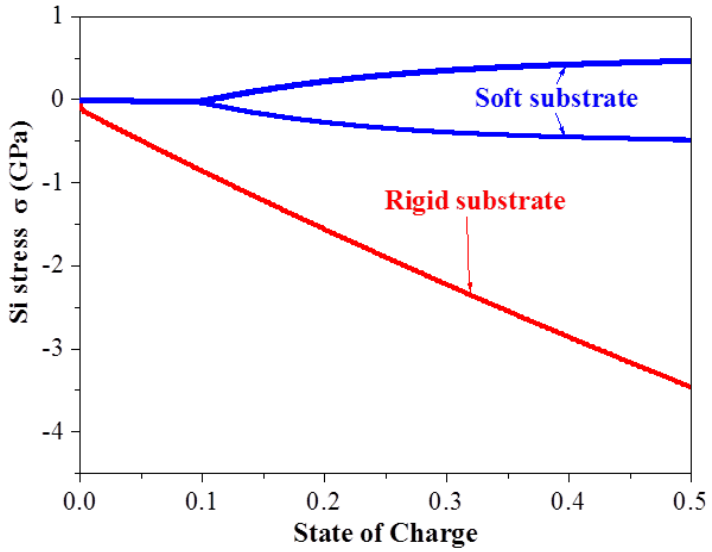

Figure 4.4. Finite element simulations show that the maximum stresses in Si are released on soft substrates, compared with the high stress developed in Si on rigid substrates.

The current system with soft substrates to release stress has very high specific charge capacity (close to the theoretical value 4,200 mAh/g as shown in Figure 5.3(b)). First-principle calculations have been conducted to explain the mechanism of high energy capacity when the stress relaxation is introduced from the energy point of

view. In the calculations, the stress relaxation is simulated by applying a tensile stress on a Li/Si system that originally has compressive stress (caused by constraints from rigid substrates). The potential energy E is given by

$$E = E_{pre} + \eta\mu_{Li} - E_{Li/Si},$$

where E_{pre} is the energy for a reference (or previously existing) Si system (with or without inserted Li), μ_{Li} is the energy for one Li atom, $E_{Li/Si}$ is the energy for the integrated Li/Si system after Li insertion, and η is the number of inserted Li atoms. The larger potential energy indicates that the Li insertion into the Si (or Si/Li) is more energetically favorable and thus the Li-inserted Si system is more energetically stable. We calculated the potential energy for inserting 160 Li atoms into a 4×4 repeated Si (111) supercell slab with 192 Si atoms. Without stress relaxation, the potential energy is calculated to be 80.94 eV and the compressive stress due to Li insertion is 10.36 GPa. To be conservative, partial stress relaxation, i.e, a 2.4 GPa tensile stress is applied to the same Li/Si system, which slightly increases Epre from -1,149.27 eV (no stress relaxation) to -1,148.03 eV (with stress relaxation). However, $E_{Li/Si}$ apparently decreases from -1,352.89 eV (no stress relaxation) to -1,360.18 eV (with stress relaxation), which increases the potential energy to 89.47 eV. This calculation indicates that the Li/Si system with stress relaxation is more energetically favorable to accommodate more Li ions, which qualitatively explains the high specific charge capacity.

4.4 Summary

In summary, the advances reported here using soft elastomeric substrates to release electrochemical reaction induced stress in Si anodes offer dramatically improved performances for Li ion batteries. Although the reported multilayered Si anodes serve to demonstrate the advantages of a half-cell battery, the same approach is fully compatible for cathode designs, which would provide unusual yet huge opportunities in high performance Li ion batteries, especially using those high energy capacity electrode materials. The fabrication process here is also compatible with standard and mature microfabrication technique, which makes this method practical for the development of high-energy thin film batteries and bulk batteries by scaling up from multilayer stacking of active materials. In addition to the electrochemical performances from the unique mechanics aspects, this technology also has the immediate potential for flexible/stretchable and portable high performance Li-ion thin film batteries based on the presented electrodes design with or without stacked layer-by-layer configurations. Besides stress relaxation, the elastomeric PDMS can also serve as solid, ion conductive, and mechanical conformable electrolyte by doping with lithium salt [130], where dual functions of PDMS make the development of high performance and solid-state thin film Li ion batteries using Si as anodes promising. We are also aware of the shortcoming of the present design, i.e., PDMS/Si electrode structure. PDMS releases the stress but also significantly increases the inactive materials, which prevents the practical application of the present method. To remove the PDMS and meanwhile be able release the stress based on the similar concept (i.e., buckling) is an on-going work that we are currently working on.

Chapter 5

Pattern transfer in submicron soft contact lithography using PDMS wrinkling Masks

We propose a near-field photolithographic approach that uses wrinkled PDMS as submicron masks to generate periodic submicron structures. The wrinkled PDMS can be easily fabricated with submicron feature sizes. When used in phase-shifting lithography, these masks produce submicron line-space pattern in photoresist transferred with large filling ratio, in contrast to generating only ~100 nm edge submicron patterns in conventional near-field soft-contact photolithography. The near-field and far-field patterns of intensity are analyzed to demonstrate the ability of pattern transferring and the advantages of large-filling-ratio line-space patterns for grating application, respectively.

5.1 Introduction

There exist many ways to fabricate submicron patterns and broadly we divide them into two technical categories: writing and replication. Most techniques used for writing submicron patterns are either too slow or too expensive to be used for mass production, such as electron beam lithography and focused ion beam. Replication of a master provides an inexpensive and convenient route in terms of mass production but still requires a submicron pattern fabricated on the master for sequential transferring inevitably involving high cost or time-consuming techniques such as high-precision writing, X-ray or EUV lithography and self-assembly.

Rogers and his colleagues used soft-contact optical lithography applying an elastomeric phase mask with feature sizes of microns to produce submicron patterns [131-135]. But this phase-shift edge lithography is limited to obtaining only shadow edge line patterns with sizes of ~100 nm and several micron loose space patterns.

We have experimentally reported a convenient near-field soft-contact photolithographic method using spontaneously formed wrinkled PDMS as optical masks for forming features with submicron sizes on photoresist [136]. In this work, we show that these patterns in photoresist can be transferred to thin metal line-space patterns using a standard liftoff procedure and also demonstrate its capability of generating submicron line-space patterning with large filling ratio. Finally we employ these periodic patterns to an application of optical diffraction grating.

5.2 Experimental

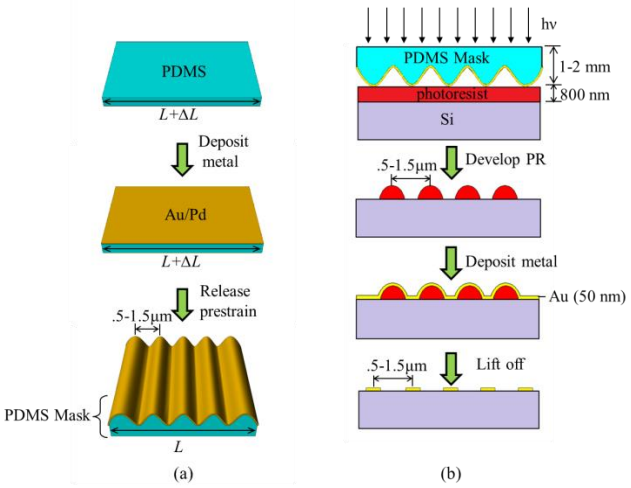

Figure. 5.1. Schematic illustrations of (a) the fabrication process for PDMS mask and (b) the lithography process with a PDMS mask.

Figure 5.1(a) outlines the procedure used to fabricate PDMS mask. The fabrication of PDMS masks is very easy and starts from a PDMS slab (1-2 mm thick). First stretch the PDMS slab and then sputter-coat a gold (90%)/palladium (10%) alloy film of nanoscale thickness atop the pre-strained PDMS. After that, release the pre-strain from PDMS gently. The relaxation of pre-strain compresses the thin alloy film leading to sinusoidal wrinkling pattern. This is a result of the minimization of the system's potential energy by integrating hard materials with soft substrate and this strategy has been proposed for various applications including stretchable electronics, tunable gratings and lithium ion batteries. Given the alloy thickness 10 nm and 50% pre-strain, the wrinkling periodicity is around 900 nm depending also on the mechanical properties of both PDMS and alloy. By varying the pre-strain and the thickness of alloy film, the wrinkling periodicity can be tuned with a broad range of hundreds nanometers to tens of microns. In this work, the wrinkling periodicity is in the order of 500-1500 nm range making it an

attractive approach for producing submicron grating (both line-width and space-width are submicron).

Figure 5.1(b) shows the use of wrinkled PDMS as a photomask in photolithography for generating submicron patterns in a thin film of positive-tone photoresist and fabricating submicron gold strips with a more lift-off step. A pre-cleaned silicon wafer is primed with hexamethyldisilazane (HMDS), spin-coated with photoresist (AZ 3312) at 6000 rpm (~800nm thick), and soft-baked at 100˚C for 1min. The PDMS mask, which is translucent to visible and UV light for the thin Au/Pd layer (10 nm), is brought into conformal contact with photoresist and an OAI 808 aligner is applied to expose the photoresist layer using ~40mJ/cm^2 of UV light (365nm) regulated by the exposure time. The exposure dose of the contact region (with the photoresist through the PDMS) is higher than that of the non-contact region due to the existence of air gap between mask and photoresist. The exposed photoresist is then removed using developer (AZ MIF 300) for 50-60 sec producing periodic structures with submicron pitch. To fabricate submicron grating the wafer is then placed in a plasma Asher for 30 sec at 200W to remove residual photoresist and a titanium/gold (5 nm/50 nm) film is subsequently deposited by e-beam evaporation. The remaining photoresist and overlying film is stripped off by a lift-off process in acetone and a submicron grating of gold stripes is obtained.

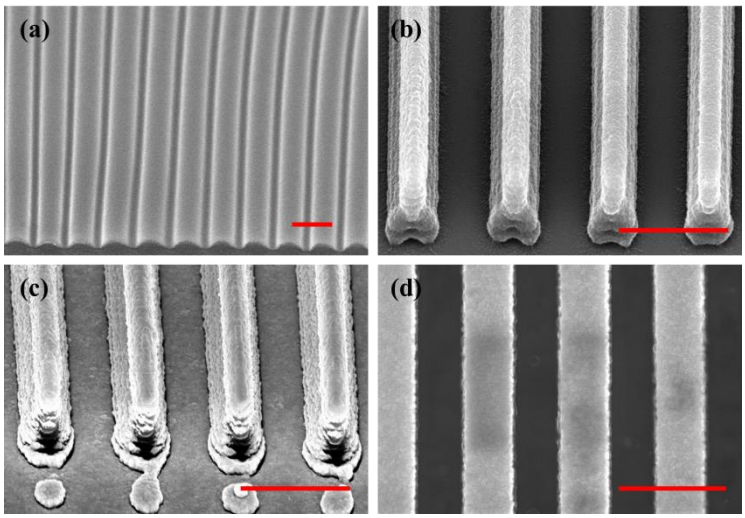

Figure 5.2. SEM image of a PDMS mask with a wrinkling periodicity of ~900 nm (a) and the patterned structures using soft-contact optical lithography with the PDMS mask: (b) Patterned photoresist; (c) 50 nm gold coated on the patterned photoresist; (d) Gold strips after a lift-off step. (The scale bar is 1μm).

Figure. 5.2(a) shows a PDMS mask with a wrinkling periodicity of ~900 nm. Photoresist strips with similar periodicity are fabricated using the soft-contact optical lithography with this mask as shown in Figure 5.2(b) and the photoresist thickness is ~800 nm. A 50-nm-thick gold layer is coated on the photoresist strips using e-beam evaporation as shown in Figure 5.2(c) and gold strips with the same pitch are generated on the substrate (Figure 5.2(d)).

5.3 Finite element analysis of near field intensity

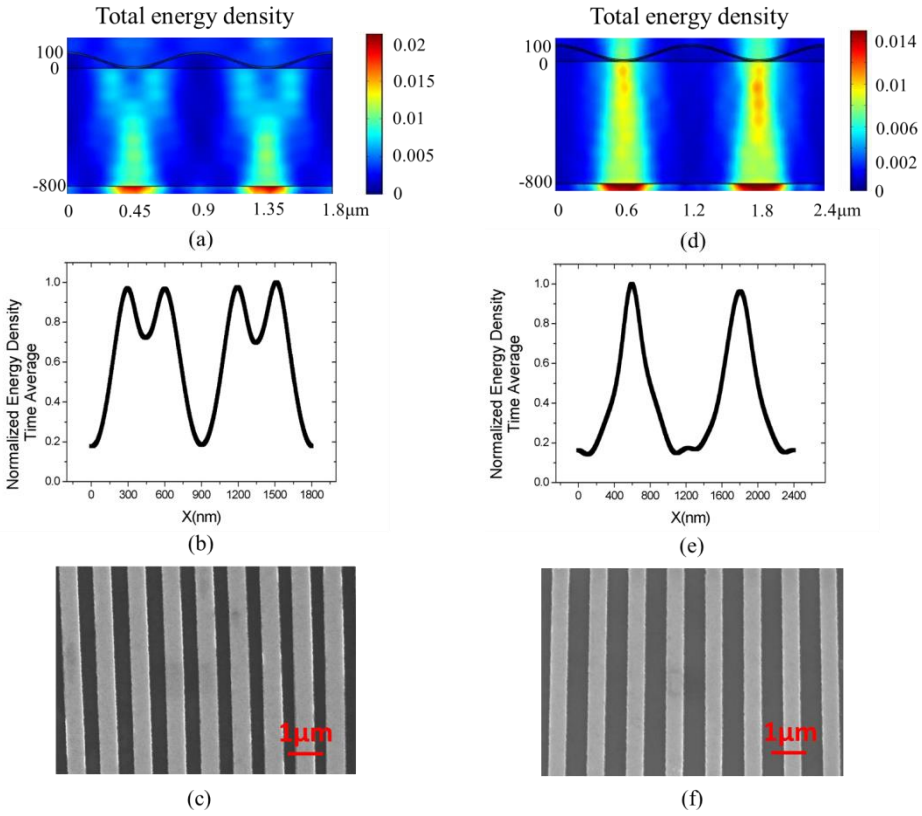

Figure 5.3. FEA simulation of near-field intensity passing through PDMS masks and the photo lithographic experiment results. Contour of energy distribution in space for a PDMS mask with a period of 900 nm (a) and 1200 nm (d), respectively. Normalized energy profile along the horizontal cut line 10 nm below the air/photoresist interface (b) from (a) and (e) from (d), respectively. SEM images of gold strips with 900 nm pitch and 1200 nm pitch fabricated using soft contact lithography with the 900 nm mask (c) and the 1200 nm mask (f), respectively. For these calculations, the wavelength of light used for exposure is 365 nm. The magnitude of the sinusoidal wrinkling pattern of the Au/Pd layer is 100 nm. The wrinkling periodicity is 900 nm. The index of refraction of the PDMS mask is 1.467.

Figure 5.3(a) and (d) illustrate the simulation results from finite element analysis (FEA) of the light intensity passing through two PDMS masks with 900 nm and 1200 nm periodicity respectively in contact with photoresist substrate. Commercial software COMSOL 4.2a is applied and the build-in 2D Electromagnetic Wave (EMW) module is used. A PDMS mask with two wrinkling periods is modeled with periodicity condition

applied at both left and right side of the model. A plane-wave light goes through the model from top to bottom. The Perfect Matching Layer (PML) is applied at the bottom of the model to avoid any unphysical refraction from the outer boundaries.

In the model, the light passes through the PDMS mask, the thin sine-shape Au/Pd layer, the air and the photoresist and generates a quasi-sinusoidal near-field pattern in the photoresist, whose periodicity matches the periodicity of the sine-wave mask, as shown in Figure 5.3(b, e). This effect only applies to the mask with submicron half-periodicity regardless of the shape of mask. As the periodicity decreases, the structure of the pattern of intensity in the near field reduces correspondingly. When the periodicity reaches a critical value of half micron (not show here) the near-field pattern simplifies to a single sinusoid. For example, a square-wave mask with submicron periodicity can generate a single sinusoid in near field as well but experimentally it is difficult to fabricate square-wave submicron pattern easily at a low cost. It is also noticed that the energy intensity reaches its highest at the region where the phase mask is in direct contact with photoresist and it drops to the lowest where there exists the highest air gap between the mask and the photoresist. This is because the air gap between the PDMS and photoresist can shift the phase of the light and therefore reduce its intensity.

This patterning capability is quite broad compared to previous edge-line-patterning in that it can transfer the shape of PDMS mask to photoresist with good fidelity and also the line-space is scalable depending on the exposure dose. But experimentally the line-width is close to the space-width in all results of photo lithography process, as shown in Figure 5.3 (c, f), which makes the structure quite suited for diffraction gratings.

5.4 Simulation for far field

We did study on the influence of the filling ratio, defined as the ratio of line-width to the pitch, of a reflective diffraction line-space grating on the grating efficiency. When a laser beam shines on the surface of a diffraction grating, the beam gets reflected and diffracted in the far field. Here the grating efficiency is defined as the ratio between the power of the first order refraction and the one of the incident light. Commercial software FDTD (finite-difference time-domain) Solution 8.7 is applied to do 2D simulation of the grating efficiency. The shape of high index bar is rectangle. The grating periodicity, the height of the high index bar, the material of each part and the incident angle of light source are all fixed during the whole calculation.

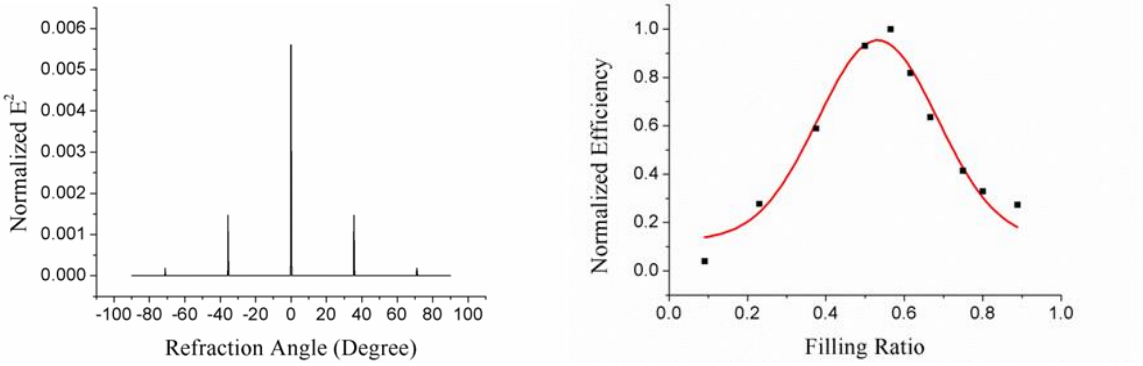

(a) (b)

Figure 5.4. Simulation plots of far-field diffraction of light reflected by a line-space grating. (a) Relationship between the square of the normalized electric field and the refraction angle. (b) shows the relationship between the normalized grating efficiency and the filling ratio. For these calculations, The wave length of the incident light is 632.8 nm, which is the typical value for the red light. The grating with 100 periods is modeled. With the magnitude of incident electrical field equals to 1 and the filling ratio of the grating equals to 0.667.

Figure 5.4 shows the simulation results for the efficiency of a reflective diffraction line-space grating. Only the first order of diffraction energy is taken account

for the grating efficiency as shown in Figure 3.4(a). In Figure 3.3(b), black dot is the raw data and red curve is the Gauss fit curve. The maximum grating efficiency can be obtained when the filling ratio is equal to about 0.5 or in other words, the line-width equals to space-width. It can be seen Gauss fit gives a good fitting of the obtained data. Therefore this soft contact lithography technique is an easy way to fabricate equal line-space patterning for the application like high efficiency diffraction grating.

5.5 Summary

In summary, we have demonstrated a convenient strategy based on soft-contact optical lithography with wrinkled PDMS mask for fabricating submicron equal line-space structures. This method has several advantages over the conventional phase-shift edge submicron lithography: the fabrication of the PDMS submicron mask is easy, low cost and no need of photo lithography; it can produce submicron features separated by submicron and the line-space width is tunable. This method also has one major limitation: it is difficult to achieve accurate control over either the feature size for masks by changing pre-strain and film thickness or the line-space ratios by varying exposure doses. Therefore, this method is a complementary approach to other photolithography and is especially suitable for generating submicron periodic patterns, where the line-width is close to the space-width but the accuracy is not critical.

CHAPTER 6

Conclusions and outlook

The last chapter summarizes this thesis work and proposed several interesting topic for future investigation.

6.1 Summary and concluding remarks

PDMS polymer is soft and elastic; Silicon, gold and ZnO are not. A strategy that overcomes this fundamental mismatch in mechanics and form has enabled exploration of a variety of applications ranging from optical grating/mask, stretchable electronics, to energy storage. Configuring such hybrid structures into "wavy" shapes yields a film/PDMS system with large stretchability and the underlying mechanism is that the wavy shapes change to accommodate applied strain resulting in considerable strains in the PDMS only, but not in the film. Here are some important accomplishments summarized from previous chapters.

The buckling instability of film/PDMS comes from the extreme mismatches in properties between PDMS and its counterpart. For example, the modulus of silicon is ~100,000 times as high as PDMS, the thickness is ~10000 times as thin, and the CTE is ~100 times as small. As a result, the buckles change their shapes to accommodate applied strains while the underlying PDMS provides an elastic restoring force. The resulting mechanical advantage, in which the peak Si strains is substantially smaller than the ribbon strains, is critical for achieving stretchability for applications including stretchable ZnO energy harvester and silicon-anode-based high performance LIB. The controlled buckling of ZnO can reach extremely high levels of stretchability (up to 60%) through selectively treating PDMS surface using a UVO mask. Although the initial state of silicon film anode in LIB is flat before charging, the silicon film upon compressing due to the electrochemical lithiation can accommodate large volume expansion and thus achieve high energy capacity. Spontaneously generated submicron PDMS/Au buckles can be firmly bonded on silicon specimen by oxygen plasma treatment for strain sensing

application and also can be utilized as photo masks to fabricate submicron periodic patterns thanks to the transparency of PDMS in a convenient and low-cost way.

6.2 Outlook of future work

Beyond the work in this thesis, the following questions remain interesting to explore in future work.

- 1D PDMS/Au wrinkling can be further extended to 2D wrinkling by applying and release 2D prestrain in both x and y direction sequentially for 2D strain sensing application.
- In addition to 1D parallel metal bars, cross-line gratings can be generated as zero-thickness spaces in both x and y directions by using PDMS/Au wrinkling as photo masks, separating tiny metal dots in a regular orthogonal array for 2D gratings. The directly fabrication processes offer a strong bonding strength between zero thickness cross-line gratings and specimen so that the thin tiny dots can deform together with the underlying specimen freely, which makes them attractive candidates for micromechanics studies involving large strain gradients or material discontinuities.
- For stretchable piezoelectric device, the fabrication of electrodes on optimized sites on PDMS is critically important but it is challenging to transfer ZnO ribbons onto electrode surface such as gold due to the weak bonding between ZnO and gold. And the piezoelectric testing of stretchable ZnO device remains poorly understood and is worth studying.

- PDMS is compliant and also transparent. It would be interesting to explore a transparent lithium ion battery, a key component for fully integrated transparent devices, which is also highly flexible by fabricating and aligning an electrode grate tens-of-micron-wide on clear PDMS.

REFERENCES

1. S. Yang, K. Khare, and P. C. Lin, "Harnessing surface wrinkle patterns in soft matter," Advanced Functional Materials **20**, 2550-2564 (2010).

2. N. Bowden, S. Brittain, A. G. Evans, J. W. Hutchinson, and G. M. Whitesides, "Spontaneous formation of ordered structures in thin films of metals supported on an elastomeric polymer," Nature **393**, 146-149 (1998).

3. J. Genzer and J. Groenewold, "Soft matter with hard skin: From skin wrinkles to templating and material characterization," Soft Matter **2**, 310-323 (2006).

4. A. Gent and I. Cho, "Surface instabilities in compressed or bent rubber blocks," Rubber Chem Technol **72**, 253-262 (1999).

5. V. Trujillo, J. Kim, and R. C. Hayward, "Creasing instability of surface-attached hydrogels," Soft Matter **4**, 564-569 (2008).

6. S. Cai, D. Chen, Z. Suo, and R. C. Hayward, "Creasing instability of elastomer films," Soft Matter **8**, 1301-1304 (2012).

7. E. Sultan and A. Boudaoud, "Statistics of crumpled paper," Phys Rev Lett **96**, 136103 (2006).

8. N. Bowden, W. T. S. Huck, K. E. Paul, and G. M. Whitesides, "The controlled formation of ordered, sinusoidal structures by plasma oxidation of an elastomeric polymer," Applied Physics Letters **75**, 2557-2559 (1999).

9. K. Efimenko, M. Rackaitis, E. Manias, A. Vaziri, L. Mahadevan, and J. Genzer, "Nested self-similar wrinkling patterns in skins," Nat Mater **4**, 293-297 (2005).

10. X. Y. Jiang, S. Takayama, X. P. Qian, E. Ostuni, H. K. Wu, N. Bowden, P. LeDuc, D. E. Ingber, and G. M. Whitesides, "Controlling mammalian cell spreading and cytoskeletal arrangement with conveniently fabricated continuous wavy features on poly(dimethylsiloxane)," Langmuir **18**, 3273-3280 (2002).

11. P. Uttayarat, G. K. Toworfe, F. Dietrich, P. I. Lelkes, and R. J. Composto, "Topographic guidance of endothelial cells on silicone surfaces with micro- to nanogrooves: Orientation of actin filaments and focal adhesions," J Biomed Mater Res A **75A**, 668-680 (2005).

12. C. H. Lu, H. Mohwald, and A. Fery, "A lithography-free method for directed colloidal crystal assembly based on wrinkling," Soft Matter **3**, 1530-1536 (2007).

13. A. Schweikart and A. Fery, "Controlled wrinkling as a novel method for the fabrication of patterned surfaces," Microchim Acta **165**, 249-263 (2009).

14. S. Wagner, S. P. Lacour, J. Jones, P.-h. I. Hsu, J. C. Sturm, T. Li, and Z. Suo, "Electronic skin: architecture and components," Physica E: Low-dimensional Systems and Nanostructures **25**, 326-334 (2004).

15. S. P. Lacour, S. Wagner, Z. Huang, and Z. Suo, "Stretchable gold conductors on elastomeric substrates," Applied physics letters **82**, 2404-2406 (2003).

16. S. P. Lacour, J. Jones, Z. Suo, and S. Wagner, "Design and performance of thin metal film interconnects for skin-like electronic circuits," Electron Device Letters, IEEE **25**, 179-181 (2004).

17. S. P. Lacour, J. Jones, S. Wagner, T. Li, and Z. Suo, "Stretchable interconnects for elastic electronic surfaces," P Ieee **93**, 1459-1467 (2005).

18. S. P. Lacour, S. Wagner, R. J. Narayan, T. Li, and Z. Suo, "Stiff subcircuit islands of diamondlike carbon for stretchable electronics," Journal of applied physics **100**, 014913-014913-014916 (2006).

19. C. Yu and H. Jiang, "Forming wrinkled stiff films on polymeric substrates at room temperature for stretchable interconnects applications," Thin Solid Films **519**, 818-822 (2010).

20. W. M. Choi, J. Song, D.-Y. Khang, H. Jiang, Y. Y. Huang, and J. A. Rogers, "Biaxially stretchable "wavy" silicon nanomembranes," Nano Lett **7**, 1655-1663 (2007).

21. D.-Y. Khang, H. Jiang, Y. Huang, and J. A. Rogers, "A stretchable form of single-crystal silicon for high-performance electronics on rubber substrates," Science **311**, 208-212 (2006).

22. H. Q. Jiang, Y. G. Sun, J. A. Rogers, and Y. G. Huang, "Mechanics of precisely controlled thin film buckling on elastomeric substrate," Applied Physics Letters **90**(2007).

23. K. M. Choi and J. A. Rogers, "A photocurable poly (dimethylsiloxane) chemistry designed for soft lithographic molding and printing in the nanometer regime," J Am Chem Soc **125**, 4060-4061 (2003).

24. H. Jiang, D.-Y. Khang, J. Song, Y. Sun, Y. Huang, and J. A. Rogers, "Finite deformation mechanics in buckled thin films on compliant supports," Proceedings of the National Academy of Sciences **104**, 15607-15612 (2007).

25. C. Yu, C. Masarapu, J. Rong, B. Wei, and H. Jiang, "Stretchable Supercapacitors Based on Buckled Single‐Walled Carbon‐Nanotube Macrofilms," Adv Mater **21**, 4793-4797 (2009).

26. C. Yu, Z. Wang, H. Yu, and H. Jiang, "A stretchable temperature sensor based on elastically buckled thin film devices on elastomeric substrates," Applied Physics Letters **95**, 141912-141912-141913 (2009).

27. C. M. Stafford, C. Harrison, K. L. Beers, A. Karim, E. J. Amis, M. R. Vanlandingham, H. C. Kim, W. Volksen, R. D. Miller, and E. E. Simonyi, "A buckling-based metrology for measuring the elastic moduli of polymeric thin films," Nat Mater **3**, 545-550 (2004).

28. J. L. Wilbur, R. J. Jackman, G. M. Whitesides, E. L. Cheung, L. K. Lee, and M. G. Prentiss, "Elastomeric optics," Chemistry of materials **8**, 1380-1385 (1996).

29. C. J. Yu, K. O'Brien, Y. H. Zhang, H. B. Yu, and H. Q. Jiang, "Tunable optical gratings based on buckled nanoscale thin films on transparent elastomeric substrates," Applied Physics Letters **96**(2010).

30. J. S. Sharp and R. A. Jones, "Micro-buckling as a route towards surface patterning," Adv Mater **14**, 799 (2002).

31. H. Schmid, H. Wolf, R. Allenspach, H. Riel, S. Karg, B. Michel, and E. Delamarche, "Preparation of metallic films on elastomeric stamps and their application for contact processing and contact printing," Advanced Functional Materials **13**, 145-153 (2003).

32. D. Y. Khang, J. A. Rogers, and H. H. Lee, "Mechanical buckling: Mechanics, metrology, and stretchable electronics," Advanced Functional Materials **19**, 1526-1536 (2009).

33. Z. Huang, W. Hong, and Z. Suo, "Nonlinear analyses of wrinkles in a film bonded to a compliant substrate," J Mech Phys Solids **53**, 2101-2118 (2005).

34. J. Groenewold, "Wrinkling of plates coupled with soft elastic media," Physica A: Statistical Mechanics and its Applications **298**, 32-45 (2001).

35. J. Song, H. Jiang, W. Choi, D. Khang, Y. Huang, and J. Rogers, "An analytical study of two-dimensional buckling of thin films on compliant substrates," Journal of Applied Physics **103**, 014303 (2008).

36. P. Chatterjee, Y. Pan, E. C. Stevens, T. Ma, H. Jiang, and L. L. Dai, "Controlled Morphology of Thin Film Silicon Integrated with Environmentally Responsive Hydrogels," Langmuir **29**, 6495-6501 (2013).

37. C. Yu, Y. Pan, H. Ma, T. Ma, J. Zhang, Y. Song, M. Y. S. Kalani, L. Dai, and H. Jiang, "Thermoresponsiveness of Integrated Ultra‐Thin Silicon with Poly (N‐isopropylacrylamide) Hydrogels," Macromol Rapid Comm **32**, 820-824 (2011).

38. P. J. Yoo, K. Y. Suh, S. Y. Park, and H. H. Lee, "Physical self-assembly of microstructures by anisotropic buckling," Adv Mater **14**, 1383-1387 (2002).

39. J. Y. Chung, T. Q. Chastek, M. J. Fasolka, H. W. Ro, and C. M. Stafford, "Quantifying residual stress in nanoscale thin polymer films via surface wrinkling," Acs Nano **3**, 844-852 (2009).

40. J. R. Serrano, Q. Xu, and D. G. Cahill, "Stress-induced wrinkling of sputtered SiO2 films on polymethylmethacrylate," Journal of Vacuum Science & Technology A **24**, 324-327 (2006).

41. T. Ma, H. Liang, G. Chen, B. Poon, H. Jiang, and H. Yu, "Micro-strain sensing using wrinkled stiff thin films on soft substrates as tunable optical grating," Opt Express **21**, 11994-12001 (2013).

42. D. Y. Khang, H. Q. Jiang, Y. Huang, and J. A. Rogers, "A stretchable form of single-crystal silicon for high-performance electronics on rubber substrates," Science **311**, 208-212 (2006).

43. Y. G. Sun, W. M. Choi, H. Q. Jiang, Y. G. Y. Huang, and J. A. Rogers, "Controlled buckling of semiconductor nanoribbons for stretchable electronics," Nature Nanotechnology **1**, 201-207 (2006).

44. T. Ma, Y. Wang, R. Tang, H. Yu, and H. Jiang, "Pre-patterned ZnO nanoribbons on soft substrates for stretchable energy harvesting applications," Journal of Applied Physics **113**, 204503 (2013).

45. J. Kim and H. H. Lee, "Wave formation by heating in thin metal film on an elastomer," Journal of Polymer Science Part B: Polymer Physics **39**, 1122-1128 (2001).

46. P. J. Yoo and H. H. Lee, "Evolution of a stress-driven pattern in thin bilayer films: spinodal wrinkling," Phys Rev Lett **91**, 154502 (2003).

47. E. P. Chan, E. J. Smith, R. C. Hayward, and A. J. Crosby, "Surface wrinkles for smart adhesion," Adv Mater **20**, 711-+ (2008).

48. E. P. Chan and A. J. Crosby, "Fabricating microlens arrays by surface wrinkling," Adv Mater **18**, 3238-3242 (2006).

49. C. Yu, X. Li, T. Ma, J. Rong, R. Zhang, J. Shaffer, Y. An, Q. Liu, B. Wei, and H. Jiang, "Silicon Thin Films as Anodes for High‐Performance Lithium‐Ion Batteries with Effective Stress Relaxation," Advanced Energy Materials **2**, 68-73 (2012).

50. R. Mukhopadhyay, "When PDMS isn't the best," Anal Chem **79**, 3248-3253 (2007).

51. T. Ohzono and H. Monobe, "Microwrinkles: Shape-tunability and applications," J Colloid Interf Sci **368**, 1-8 (2012).

52. C. M. Chen and S. Yang, "Wrinkling instabilities in polymer films and their applications," Polym Int **61**, 1041-1047 (2012).

53. W. N. Sharpe Jr and W. N. Sharpe, *Springer handbook of experimental solid mechanics* (Springer, 2008).

54. J. D. Wood, P. Sobolewski, V. Thakur, D. Arola, A. Nazari, F. R. Tay, and D. H. Pashley, "Measurement of microstrains across loaded resin-dentin interfaces using microscopic moire interferometry," Dental Materials **24**, 859-866 (2008).

55. B. Chen and C. Basaran, "Automatic full strain field Moire interferometry measurement with nano-scale resolution," Exp. Mech. **48**, 665-673 (2008).

56. B. Han and Y. Guo, "Thermal deformation analysis of various electronic packaging products by Moire and microscopic Moire interferometry," J. Electron. Packag. **117**, 185-191 (1995).

57. C. M. Liu and L. W. Chen, "Digital atomic force microscope Moire method," Ultramicroscopy **101**, 173-181 (2004).

58. J. McKelvie, "Moire strain analysis: an introduction, review and critique, including related techniques and future potential," Journal of Strain Analysis for Engineering Design **33**, 137-151 (1998).

59. Y. H. Zhou, B. Pan, and Y. Q. Chen, "Large deformation measurement using digital image correlation: a fully automated approach," Applied Optics **51**, 7674-7683 (2012).

60. C. Cofaru, W. Philips, and W. Van Paepegem, "Pixel-level robust digital image correlation," Optics Express **21**, 29979-29999 (2013).

61. D. Spera, K. Genovese, and A. Voloshin, "Application of Stereo-Digital Image Correlation to Full-Field 3-D Deformation Measurement of Intervertebral Disc," Strain **47**, E572-E587 (2011).

62. M. A. Sutton, J. H. Yan, V. Tiwari, H. W. Schreier, and J. J. Orteu, "The effect of out-of-plane motion on 2D and 3D digital image correlation measurements," Opt. Lasers Eng. **46**, 746-757 (2008).

63. H. Lu and P. D. Cary, "Deformation measurements by digital image correlation: Implementation of a second-order displacement gradient," Exp. Mech. **40**, 393-400 (2000).

64. A. U. Manual, "Version 6.5, Hibbitt, Karlsson and Sorensen," Inc., Pawtucket, RI (2004).

65. R. Li, Y. Li, L. Chaofeng, J. Song, R. Saeidpouraza, B. Fang, Y. Zhong, P. M. Ferreira, J. A. Rogers, and Y. Huang, "Thermo-mechanical modeling of laser-driven non-contact transfer printing: two-dimensional analysis," Soft Matter (2012).

66. C. S. Selvanayagam, J. H. Lau, X. Zhang, S. Seah, K. Vaidyanathan, and T. Chai, "Nonlinear thermal stress/strain analyses of copper filled TSV (through silicon via) and their flip-chip microbumps," Advanced Packaging, IEEE Transactions on **32**, 720-728 (2009).

67. B. H. Jo, L. M. Van Lerberghe, K. M. Motsegood, and D. J. Beebe, "Three-dimensional micro-channel fabrication in polydimethylsiloxane (PDMS) elastomer," Microelectromechanical Systems, Journal of **9**, 76-81 (2000).

68. D. Post, B. Han, and P. Ifju, *High sensitivity moiré: experimental analysis for mechanics and materials* (Springer, 1997).

69. P. Ifju and D. Post, "ZERO‐THICKNESS SPECIMEN GRATINGS FOR MOIRE INTERFEROMETRY," Exp Techniques **15**, 45-47 (1991).

70. Y. Qi, N. T. Jafferis, K. Lyons, C. M. Lee, H. Ahmad, and M. C. McAlpine, "Piezoelectric Ribbons Printed onto Rubber for Flexible Energy Conversion," Nano Lett **10**, 524-528 (2010).

71. X. Feng, B. D. Yang, Y. M. Liu, Y. Wang, C. Dagdeviren, Z. J. Liu, A. Carlson, J. Y. Li, Y. G. Huang, and J. A. Rogers, "Stretchable Ferroelectric Nanoribbons with Wavy Configurations on Elastomeric Substrates," ACS Nano **5**, 3326-3332 (2011).

72. Y. Qi, J. Kim, T. D. Nguyen, B. Lisko, P. K. Purohit, and M. C. McAlpine, "Enhanced Piezoelectricity and Stretchability in Energy Harvesting Devices Fabricated from Buckled PZT Ribbons," Nano Lett **11**, 1331-1336 (2011).

73. T. D. Nguyen, N. Deshmukh, J. M. Nagarah, T. Kramer, P. K. Purohit, M. J. Berry, and M. C. McAlpine, "Piezoelectric nanoribbons for monitoring cellular deformations," Nat. Nanotechnol. **7**, 587-593 (2012).

74. K. I. Park, S. Xu, Y. Liu, G. T. Hwang, S. J. L. Kang, Z. L. Wang, and K. J. Lee, "Piezoelectric BaTiO3 Thin Film Nanogenerator on Plastic Substrates," Nano Lett. **10**, 4939-4943 (2010).

75. K. I. Park, S. Y. Lee, S. Kim, J. Chang, S. J. L. Kang, and K. J. Lee, "Bendable and Transparent Barium Titanate Capacitors on Plastic Substrates for High Performance Flexible Ferroelectric Devices," Electrochem Solid St **13**, G57-G59 (2010).

76. H. C. Seo, I. Petrov, H. Jeong, P. Chapman, and K. Kim, "Elastic buckling of AlN ribbons on elastomeric substrate," Appl. Phys. Lett. **94**, 092104 (2009).

77. Z. L. Wang and J. H. Song, "Piezoelectric nanogenerators based on zinc oxide nanowire arrays," Science **312**, 242-246 (2006).

78. R. Yang, Y. Qin, C. Li, G. Zhu, and Z. L. Wang, "Converting Biomechanical Energy into Electricity by a Muscle-Movement-Driven Nanogenerator," Nano Lett **9**, 1201-1205 (2009).

79. R. S. Yang, Y. Qin, L. M. Dai, and Z. L. Wang, "Power generation with laterally packaged piezoelectric fine wires," Nature Nanotechnology **4**, 34-39 (2009).

80. S. Xu, Y. Qin, C. Xu, Y. G. Wei, R. S. Yang, and Z. L. Wang, "Self-powered nanowire devices," Nat. Nanotechnol. **5**, 366-373 (2010).

81. L. Baeten, B. Conings, H. G. Boyen, J. D'Haen, A. Hardy, M. D'Olieslaeger, J. V. Manca, and M. K. Van Bael, "Towards efficient hybrid solar cells based on fully polymer infiltrated ZnO nanorod arrays," Adv Mater **23**, 2802-2805 (2011).

82. Y. Li, P. Lu, M. Jiang, R. Dhakal, P. Thapaliya, Z. Peng, B. Jha, and X. Yan, "Femtosecond Time-Resolved Fluorescence Study of TiO2-Coated ZnO Nanorods/P3HT Photovoltaic Films," The Journal of Physical Chemistry C **116**, 25248-25256 (2012).

83. X. D. Bai, P. X. Gao, Z. L. Wang, and E. G. Wang, "Dual-mode mechanical resonance of individual ZnO nanobelts," Appl. Phys. Lett. **82**, 4806-4808 (2003).

84. J. Casals-Terre, A. Fargas-Marques, and A. M. Shkel, "Snap-Action Bistable Micromechanisms Actuated by Nonlinear Resonance," J. Microelectromech. Syst. **17**, 1082-1093 (2008).

85. F. Cottone, H. Vocca, and L. Gammaitoni, "Nonlinear Energy Harvesting," Phys. Rev. Lett. **102**, 080601 (2009).

86. A. F. Arrieta, P. Hagedorn, A. Erturk, and D. J. Inman, "A piezoelectric bistable plate for nonlinear broadband energy harvesting," Appl. Phys. Lett. **97**, 104102 (2010).

87. S. M. Jung and K. S. Yun, "Energy-harvesting device with mechanical frequency-up conversion mechanism for increased power efficiency and wideband operation," Appl. Phys. Lett. **96**, 111906 (2010).

88. N. A. Khovanova and I. A. Khovanov, "The role of excitations statistic and nonlinearity in energy harvesting from random impulsive excitations," Appl. Phys. Lett. **99**, 144101 (2011).

89. F. Cottone, L. Gammaitoni, H. Vocca, M. Ferrari, and V. Ferrari, "Piezoelectric buckled beams for random vibration energy harvesting," Smart Mater. Struct. **21**, 035021 (2012).

90. Y. Wang, T. Ma, H. Yu, and H. Jiang, "Random analysis on controlled buckling structure for energy harvesting," Applied Physics Letters **102**, 041915-041915-041915 (2013).

91. D. C. Duffy, J. C. McDonald, O. J. A. Schueller, and G. M. Whitesides, "Rapid prototyping of microfluidic systems in poly(dimethylsiloxane)," Analytical Chemistry **70**, 4974-4984 (1998).

92. M. Ouyang, C. Yuan, R. J. Muisener, A. Boulares, and J. T. Koberstein, "Conversion of some siloxane polymers to silicon oxide by UV/ozone photochemical processes," Chemistry of Materials **12**, 1591-1596 (2000).

93. W. R. Childs, M. J. Motala, K. J. Lee, and R. G. Nuzzo, "Masterless soft lithography: Patterning UV/ozone-induced adhesion on poly(dimethylsiloxane) surfaces," Langmuir **21**, 10096-10105 (2005).

94. A. Bietsch and B. Michel, "Conformal contact and pattern stability of stamps used for soft lithography," J. Appl. Phys. **88**, 4310-4318 (2000).

95. G. Mantini, Y. F. Gao, A. D'Amico, C. Falconi, and Z. L. Wang, "Equilibrium Piezoelectric Potential Distribution in a Deformed ZnO Nanowire," Nano Res. **2**, 624-629 (2009).

96. H. Jiang, Y. Sun, J. A. Rogers, and Y. Y. Huang, "Mechanics of Precisely Controlled Thin Film Buckling on Elastomeric Substrate," Appl. Phys. Lett. **90**, 133119 (2007).

97. Y. Wang and X. Feng, "Dynamic behaviors of controllably buckled thin films," Appl. Phys. Lett. **95**, 231915 (2009).

98. B. Boukamp, G. Lesh, and R. Huggins, "All ‐ solid lithium electrodes with mixed ‐ conductor matrix," J Electrochem Soc **128**, 725-729 (1981).

99. J. R. Szczech and S. Jin, "Nanostructured silicon for high capacity lithium battery anodes," Energ Environ Sci **4**, 56-72 (2011).

100. R. Huggins and W. Nix, "Decrepitation model for capacity loss during cycling of alloys in rechargeable electrochemical systems," Ionics **6**, 57-63 (2000).

101. J. H. Ryu, J. W. Kim, Y.-E. Sung, and S. M. Oh, "Failure modes of silicon powder negative electrode in lithium secondary batteries," Electrochemical and solid-state letters **7**, A306-A309 (2004).

102. U. Kasavajjula, C. Wang, and A. J. Appleby, "Nano-and bulk-silicon-based insertion anodes for lithium-ion secondary cells," J Power Sources **163**, 1003-1039 (2007).

103. T. Takamura, S. Ohara, M. Uehara, J. Suzuki, and K. Sekine, "A vacuum deposited Si film having a Li extraction capacity over 2000 mAh/g with a long cycle life," Journal of Power Sources **129**, 96-100 (2004).

104. H. Ma, F. Y. Cheng, J. Chen, J. Z. Zhao, C. S. Li, Z. L. Tao, and J. Liang, "Nest-like silicon nanospheres for high-capacity lithium storage," Advanced Materials **19**, 4067-+ (2007).

105. H. Kim, B. Han, J. Choo, and J. Cho, "Three-Dimensional Porous Silicon Particles for Use in High-Performance Lithium Secondary Batteries," Angewandte Chemie-International Edition **47**, 10151-10154 (2008).

106. Y.-L. Kim, Y.-K. Sun, and S.-M. Lee, "Enhanced electrochemical performance of silicon-based anode material by using current collector with modified surface morphology," Electrochim Acta **53**, 4500-4504 (2008).

107. X. Wang, Z. Wen, Y. Liu, and X. Wu, "A novel composite containing nanosized silicon and tin as anode material for lithium ion batteries," Electrochim Acta **54**, 4662-4667 (2009).

108. Q. Si, K. Hanai, N. Imanishi, M. Kubo, A. Hirano, Y. Takeda, and O. Yamamoto, "Highly reversible carbon ‐ nano-silicon composite anodes for lithium rechargeable batteries," J Power Sources **189**, 761-765 (2009).

109. Y. Liu, Z. Wen, X. Wang, X. Yang, A. Hirano, N. Imanishi, and Y. Takeda, "Improvement of cycling stability of Si anode by mechanochemcial reduction and carbon coating," J Power Sources **189**, 480-484 (2009).

110. C. K. Chan, H. L. Peng, G. Liu, K. McIlwrath, X. F. Zhang, R. A. Huggins, and Y. Cui, "High-performance lithium battery anodes using silicon nanowires," Nature Nanotechnology **3**, 31-35 (2008).

111. L.-F. Cui, Y. Yang, C.-M. Hsu, and Y. Cui, "Carbon− silicon core− shell nanowires as high capacity electrode for lithium ion batteries," Nano Lett **9**, 3370-3374 (2009).

112. H. Kim and J. Cho, "Superior lithium electroactive mesoporous Si@ Carbon core− shell nanowires for lithium battery anode material," Nano Lett **8**, 3688-3691 (2008).

113. M.-H. Park, M. G. Kim, J. Joo, K. Kim, J. Kim, S. Ahn, Y. Cui, and J. Cho, "Silicon nanotube battery anodes," Nano Lett **9**, 3844-3847 (2009).

114. T. Song, J. Xia, J.-H. Lee, D. H. Lee, M.-S. Kwon, J.-M. Choi, J. Wu, S. K. Doo, H. Chang, and W. I. Park, "Arrays of sealed silicon nanotubes as anodes for lithium ion batteries," Nano Lett **10**, 1710-1716 (2010).

115. D.-H. Kim, J.-H. Ahn, W. M. Choi, H.-S. Kim, T.-H. Kim, J. Song, Y. Y. Huang, Z. Liu, C. Lu, and J. A. Rogers, "Stretchable and foldable silicon integrated circuits," Science **320**, 507-511 (2008).

116. J. Viventi, D.-H. Kim, J. D. Moss, Y.-S. Kim, J. A. Blanco, N. Annetta, A. Hicks, J. Xiao, Y. Huang, and D. J. Callans, "A conformal, bio-interfaced class of silicon electronics for mapping cardiac electrophysiology," Science translational medicine **2**, 24ra22-24ra22 (2010).

117. R. Deslattes, A. Henins, H. Bowman, R. Schoonover, C. Carroll, I. Barnes, L. Machlan, L. Moore, and W. Shields, "Determination of the Avogadro constant," Phys Rev Lett **33**, 463-466 (1974).

118. Y. Liu, T. Matsumura, N. Imanishi, A. Hirano, T. Ichikawa, and Y. Takeda, "Preparation and Characterization of Si ／ C Composite Coated with Polyaniline as Novel Anodes for Li-Ion Batteries," Electrochemical and Solid-State Letters **8**, A599-A602 (2005).

119. K. Zhao, M. Pharr, S. Cai, J. J. Vlassak, and Z. Suo, "Large Plastic Deformation in High‐Capacity Lithium‐Ion Batteries Caused by Charge and Discharge," J Am Ceram Soc **94**, s226-s235 (2011).

120. K. Zhao, M. Pharr, J. J. Vlassak, and Z. Suo, "Inelastic hosts as electrodes for high-capacity lithium-ion batteries," Journal of Applied Physics **109**, 016110 (2011).

121. K. Zhao, W. L. Wang, J. Gregoire, M. Pharr, Z. Suo, J. J. Vlassak, and E. Kaxiras, "Lithium-assisted plastic deformation of silicon electrodes in lithium-ion batteries: a first-principles theoretical study," Nano Lett **11**, 2962-2967 (2011).

122. T. K. Bhandakkar and H. Gao, "Cohesive modeling of crack nucleation under diffusion induced stresses in a thin strip: Implications on the critical size for flaw tolerant battery electrodes," Int J Solids Struct **47**, 1424-1434 (2010).

123. Y. Liu, K. Hanai, J. Yang, N. Imanishi, A. Hirano, and Y. Takeda, "Silicon/carbon composites as anode materials for Li-ion batteries," Electrochemical and solid-state letters **7**, A369-A372 (2004).

124. Q. Si, K. Hanai, T. Ichikawa, A. Hirano, N. Imanishi, Y. Takeda, and O. Yamamoto, "A high performance silicon/carbon composite anode with carbon nanofiber for lithium-ion batteries," J Power Sources **195**, 1720-1725 (2010).

125. W.-J. Zhang, "Lithium insertion/extraction mechanism in alloy anodes for lithium-ion batteries," J Power Sources **196**, 877-885 (2011).

126. V. A. Sethuraman, V. Srinivasan, A. F. Bower, and P. R. Guduru, "In situ measurements of stress-potential coupling in lithiated silicon," J Electrochem Soc **157**, A1253-A1261 (2010).

127. J. Y. Huang, L. Zhong, C. M. Wang, J. P. Sullivan, W. Xu, L. Q. Zhang, S. X. Mao, N. S. Hudak, X. H. Liu, and A. Subramanian, "In situ observation of the electrochemical lithiation of a single SnO2 nanowire electrode," Science **330**, 1515-1520 (2010).

128. V. A. Sethuraman, M. J. Chon, M. Shimshak, V. Srinivasan, and P. R. Guduru, "< i> In situ</i> measurements of stress evolution in silicon thin films during electrochemical lithiation and delithiation," J Power Sources **195**, 5062-5066 (2010).

129. S. K. Soni, B. W. Sheldon, X. Xiao, and A. Tokranov, "Thickness effects on the lithiation of amorphous silicon thin films," Scripta Mater **64**, 307-310 (2011).

130. Q. Hu, S. Osswald, R. Daniel, Y. Zhu, S. Wesel, L. Ortiz, and D. R. Sadoway, "Graft copolymer-based lithium-ion battery for high-temperature operation," J Power Sources **196**, 5604-5610 (2011).

131. T. W. Lee, S. Jeon, J. Maria, J. Zaumseil, J. W. Hsu, and J. A. Rogers, "Soft‐Contact Optical Lithography Using Transparent Elastomeric Stamps and Application to Nanopatterned Organic Light‐Emitting Devices," Advanced functional materials **15**, 1435-1439 (2005).

132. J. A. Rogers, K. E. Paul, R. J. Jackman, and G. M. Whitesides, "Using an elastomeric phase mask for sub-100 nm photolithography in the optical near field," Applied Physics Letters **70**, 2658-2660 (1997).

133. D. Qin, Y. Xia, A. J. Black, and G. M. Whitesides, "Photolithography with transparent reflective photomasks," J Vac Sci Technol B **16**, 98-103 (1998).

134. Z.-Y. Li, Y. Yin, and Y. Xia, "Optimization of elastomeric phase masks for near-field photolithography," Applied Physics Letters **78**, 2431-2433 (2001).

135. J. A. Rogers, K. E. Paul, R. J. Jackman, and G. M. Whitesides, "Generating~ 90 nanometer features using near-field contact-mode photolithography with an elastomeric phase mask," Journal of Vacuum Science and Technology-Section B-Microelectronics Nanometer Structur **16**, 59-68 (1998).

136. K. Chen, E. Azhar, T. Ma, H. Jiang, and H. Yu, "Facile large-area photolithography of periodic sub-micron structures using a self-formed polymer mask," Applied Physics Letters **100**, 233503 (2012).

APPENDIX A

COPYRIGHT

This thesis includes some of my own published work. The detailed copyright permission is showing as below.

Chapter 2 is reproduced with permission from Teng Ma[*], Hanshuang Liang[*], George Chen, Benny Poon, Hanqing Jiang, and Hongbin Yu. "Micro-strain sensing using wrinkled stiff thin films on soft substrates as tunable optical grating." Optics Express 21.10 (2013): 11994-12001. ([*]: Equal contribution). Copyright © 2013 The Optical Society.

Chapter 2 is also reproduced with permission from Hanshuang Liang[*], Teng Ma[*], Hoa Nguyen, George Chen, Hao Wu, Hanqing Jiang, and Hongbin Yu. "High Sensitivity In-Plane Strain Measurement Using a Laser Scanning Technique." Electronic Components and Technology Conference (ECTC), 2014 IEEE 64rd. IEEE, 2014. ([*]: Equal contribution). Copyright © 2014 IEEE.

Chapter 3 is reproduced with permission from Teng Ma, Yong Wang, Rui Tang, Hongyu Yu, and Hanqing Jiang. "Pre-patterned ZnO nanoribbons on soft substrates for stretchable energy harvesting applications." Journal of Applied Physics 113.20 (2013): 204503. Copyright © 2013 American Institute of Physics.

Chapter 4 is reproduced with permission from Cunjiang Yu, Xin Li, Teng Ma, Jiepeng Rong, Rongjun Zhang, Joseph Shaffer, Yonghao An, Qiang Liu, Bingqing Wei, and Hanqing Jiang. "Silicon Thin Films as Anodes for High‐Performance Lithium‐Ion Batteries with Effective Stress Relaxation." Advanced Energy Materials 2.1 (2012): 68-73. Copyright © 2012 John Wiley & Sons.

APPENDIX B

CO-AUTHOR APPROVAL

I verify that the following co-authors have approved the usage of our publication materials in the thesis:

Hanqing Jiang (Arizona State University)

Hongbin Yu (Arizona State University)

Benny Poon (Intel Corp.)

Hanshuang Liang (Arizona State University)

George Chen (Arizona State University)

Cheng Lv (Arizona State University)

Hoa Nguyen (Arizona State University)

Hao Wu (Arizona State University)

Rui Tang (Arizona State University)

Hongyu Yu (Arizona State University)

Yong Wang (Zhejiang University)

Cunjiang Yu (Arizona State University)

Rongjun Zhang (Arizona State University)

Joseph Shaffer (Arizona State University)

Yonghao An (Arizona State University)

Qiang Liu (Arizona State University)

Bingqing Wei (University of Delaware)

Xin Li (University of Delaware)

Jiepeng Rong (University of Delaware)